Elasticity of selected icy satellite candidate materials (CO_2, C_6H_6, $MgSO_4 \cdot 7H_2O$ and $CaSO_4 \cdot 2H_2O$) revisited by dispersion corrected density functional theory

Johannes M. Meusburger[1,2,3], Karen A. Hudson-Edwards[1], Chiu C. Tang[2], Rich A. Crane[1], A. Dominic Fortes[3,*]

[1] Camborne School of Mines and Environment and Sustainability Institute, Tremough Campus, University of Exeter, Penryn TR10 9EZ, UK

[2] Diamond Light Source, Harwell Science and Innovation Campus, Fermi Avenue, Didcot OX11 0DE, UK

[3] ISIS Neutron and Muon Source, STFC Rutherford Appleton Laboratory, Harwell Science and Innovation Campus, Chilton, Didcot, Oxfordshire, OX11 0QX, UK

*corresponding author

Keywords: icy ocean worlds, interiors, elasticity, seismic exploration, density functional theory

Highlights

- Elasticity of four icy satellite candidate materials explored by DFT + D
- Improvement over non-dispersion corrected DFT
- Dispersion dominated compounds better modelled than hydrogen bonded
- Bulk compressibility well approximated
- Large differences for elastic anisotropy and seismic wave speed

Abstract

Seismic studies are essential for accurate characterisation of planetary interior structures, but are dependent on modelling for interpretation, requiring data on the elastic properties of likely constituent minerals. With the potential deployment of seismic stations on icy worlds such as Europa and Titan envisioned for the near future, a campaign of study into the elasticity of potential icy ocean world minerals is of paramount importance.

In the paper we assess the role of first-principles computer simulations to this problem, in particular focussing on the application of recent advances in simulating dispersion forces in loosely-bonded molecular solids, likely to be the main constituents of icy ocean worlds. This is of particular interest for these kinds of materials, since the complex sample handling, phase transitions and the difficulty of obtaining single crystals often greatly complicates the experimental determination of the full elastic tensor.

We focus on CO_2, C_6H_6, $MgSO_4 \cdot 7H_2O$ and $CaSO_4 \cdot 2H_2O$ as they allow us to benchmark the performance over a wide range of chemical space, structural topologies, crystal symmetries and bonding types, and moreover have accurate experimentally determined unit-cell dimensions, bulk moduli and full elastic tensors for benchmarking purposes.

We demonstrate that the dispersion corrected approaches indeed perform superior in modelling the experimental density profiles (mean unsigned differences of merely 0.04 g/cm^3 (CO_2), 0.02 g/cm^3 (C_6H_6), 0.003 g/cm^3 ($MgSO_4 \cdot 7H_2O$) and 0.013 g/cm^3 ($CaSO_4 \cdot 2H_2O$)) and may find application in exploring the compressive parameters of candidate materials, which could then be used in rheological models of icy ocean worlds.

Moreover, we have assessed if the elastic constants computed by dispersion corrected density functional theory are accurate enough to be used in a reference data base for the seismic exploration of icy ocean worlds. Despite one approach having demonstrated good accuracy compared with the experimental values in modelling the elasticity of CO_2, we instead find average differences from expected P and S wave velocities of around 10 to 25 % for the elastically more complex title compounds. In part these differences are due to the large temperature difference between the experimental elasticity data (typically near 300 K) and our calculations, which were performed in the athermal limit.

1. Introduction

The outer solar system harbours numerous planetary objects of diverse internal and surface structure. The Voyager, Galileo, Cassini and New Horizon missions found indications that some of these objects (e.g. Europa, Ganymede, Callisto, Enceladus, Titan, Triton and Pluto; Nimmo, 2018) may conceal subsurface oceans beneath an icy surface and are thus referred to collectively as icy ocean worlds (IOW). The possibility of sustaining a liquid ocean concealed beneath an icy crust clearly makes them a prime target for the search for extra-terrestrial life.

Present models of the interior of IOW are based on knowledge about their mass, diameter, and low-order gravity-field harmonics as determined during close flybys in spacecraft missions (Monteux et al., 2018; Nimmo, 2018). In addition, high-resolution images acquired in such spacecraft missions provide insight into the surface geology which in turn may be used to infer IOW's thermal history (e.g. Bland et al., 2012). Unsurprisingly, remote sensing based models are associated with a high degree of uncertainty, making it difficult to constrain key habitability parameters (e.g. depth, ocean pressure, temperature and chemistry) accurately enough to assess the astrobiological potential of these proclaimed subsurface oceans. In order to draw a detailed picture of the internal structure of icy satellites, *in situ* geophysical exploration methods such as seismology appear to be the method of choice, thus the proposed Europa (Pappalardo et al., 2013) and the recently selected Titan (New Frontiers Dragonfly, Lorenz et al., 2018) lander missions both include a single station seismometer in their proposed scientific payload. Single station seismometers have most recently found application in the successful exploration of the interior of comet 67P/Churyumov–Gerasimenko (Philae mission; Knapmeyer et al., 2017) and Mars (InSight mission), and in the latter case have even enabled determination of both the core radius (Stähler et al., 2021) and crustal thickness (Drilleau et al., 2021).

Despite recent application on other celestial bodies, seismology has been, first and foremost, a technique to study the Earth and has greatly advanced our knowledge of its interior (e.g. Mohorovičić, 1910;

72 Lehmann, 1936; Stephenson et al., 2020). The successful mineral identification by means of seismology,
73 however, is reliant upon the use of accurate reference elasticity data of promising candidate mineral phases.
74 Due to the difficulties associated with the seismic exploration of celestial bodies, the obvious focus of mineral
75 physicists has been the study of the elastic properties of silicate minerals which account for the bulk of the
76 terrestrial mantle and crust (Ringwood, 1969). Minerals which constitute the icy mantle of IOW are presumed
77 to be various ice polymorphs, chondritic salts (e.g. sulfate and chloride minerals) and acids (e.g. sulfuric acid
78 and its hydrates), and primitive volatiles (e.g. NH_4, CO_2, hydrocarbons, N_2; Fortes & Choukroun, 2010). The
79 elastic properties of many of such phases are poorly constrained or in some instances completely unknown.
80 This current gap in the literature therefore acts as a barrier against the efficacy of a likely future deployment
81 of a seismometer on an IOW.

82 The determination of elastic constants is further complicated by the pressure and temperature
83 dependency of the elastic tensor, the wide range of pressure (i.e. ~ 0 - 3.45 GPa; with the upper bound
84 corresponding to Callisto's central pressure assuming a partly differentiated model for the internal structure
85 (Prentice, 1999)) and temperature conditions (~ 25 - 450 K, with the upper and lower bound corresponding to
86 the melting temperature of ice VII at ~3.5 GPa (Dubrovinsky & Dubrovinskaya, 2007) and the minimum
87 surface temperature of Pluto and other Kuiper belt objects (Earle et al., 2017), respectively) the candidate
88 phases may be subjected to in the icy mantle. Considering the large number of candidate phases and the
89 complexity of the experiments involved, the exploration of the elastic constants including their pressure and
90 temperature dependency would be a rather ambitious endeavour. Further complicating these experiments are
91 the complex high-pressure high-temperature phase relations involving incongruent melting (e.g. Comodi et al.,
92 2017; Fortes et al., 2017; Gromnitskaya et al., 2013; Wang et al., 2018) and polymorphic phase transitions
93 (e.g. Ende et al., 2020; Meusburger et al., 2019, 2020) as well as the difficult sample handling due to re- or

dehydration induced by changes in relative humidity as observed for numerous candidate phases (Wang et al., 2016).

An alternative approach to estimate elastic constants is computation from quantum mechanical first principles, such as within the framework of density functional theory (DFT) (Hohenberg & Kohn, 1964; Kohn & Sham, 1965), as this circumvents the problems associated with sample handling, albeit at the expense of experimental accuracy. One of the major shortcomings of all local and semi-local density functional approximations is the failure to model long-range intermolecular interactions, commonly referred to as London dispersion forces, accurately (Tkatchenko & Scheffler, 2009). Due to the critical role London dispersion forces play in a plethora of materials, many of them being of technological interest, considerable effort has been put into the development of dispersion correction schemes. The accurate treatment of dispersion forces is regarded as one of the most recent success stories in the field of DFT (Burke, 2012) and has resulted in an improved accuracy for numerous loosely packed solids such as metal organic framework (Formalik et al., 2018) , zeolites (Fischer & Angel, 2017) and organic molecular crystals (Winkler & Milman, 2019). Most importantly from a planetary scientist's perspective, the improved modelling of dispersion forces also opens the door for improved accuracy in the computational exploration of the material properties of IOW candidate phases, many of which are dispersion dominated loosely-bonded solids.

In order to test this hypothesis we have assessed the performance of various dispersion correction schemes to model crystal structures and high-pressure behaviour of selected icy satellite candidate phases (i.e. CO_2, C_6H_6, $MgSO_4 \cdot 7H_2O$ and $CaSO_4 \cdot 2H_2O$). These include the D2 scheme (Grimme, 2006), the TS scheme (Tkatchenko & Scheffler, 2009) and the many-body dispersion method with range-separated screening (commonly abbreviated as MBD@rsSCS but named MBD hereafter for the sake of brevity, Ambrosetti et al., 2014) in conjunction with the Perdew–Burke-Ernzerhof (PBE; Perdew et al., 1996) and Perdew–Burke-Ernzerhof dedicated solid state (PBEsol; Perdew et al., 2008) exchange correlation (xc) functionals. The best

117 performing combination of functional and dispersion correction, as well as the PBEsol xc functional, which is
118 regarded as yielding accurate elastic tensor (Winkler & Milman, 2014), will then be applied to compute the
119 full elastic tensor. The results will be evaluated against each other and compared with literature data.

120 We focus on CO_2, C_6H_6, $MgSO_4 \cdot 7H_2O$ and $CaSO_4 \cdot 2H_2O$ as they allow us to benchmark the
121 performance over a wide range of chemical space, structural topologies, crystal symmetries and bonding types,
122 and moreover have accurate experimentally determined unit-cell dimensions, bulk moduli and full elastic
123 tensors for benchmarking purposes. Finally, we assess the role that dispersion corrected DFT may play in
124 exploring the elasticity of candidate phases. In particular, we want to assess if the elastic constants computed
125 by dispersion corrected DFT are accurate enough to be used in a reference data base for the seismic exploration
126 of IOWs. Such a database would allow for a seismic exploration of IOW, ideally casting light on the icy mantle
127 dynamics and chemical fluxes into and out of the ocean, both of them being key parameters in assessing
128 habitability.
129

2. Methods

2.1. Set up of DFT calculations

A series of plane-wave pseudopotential DFT calculations were carried using the CASTEP code (Clark et al., 2005) version 17.2.1. Input files were generated in the BIOVIA Materials studio software. The calculations were subsequently run according to following geometry optimisation strategy: After initial structural relaxations using a plane-wave cut-off of 800 eV, starting from the experimentally determined geometries obtained from the literature (Tab. 1), single point energy calculations for various basis set sampling grids and cut-off energies ranging from 500-1400 eV were performed (supplementary material: Fig. s1a-d). Converged basis set parameters (i.e. plane wave cut-off energy and Monkhost-Pack k-points; Monkhorst & Pack, 1976) were derived from these calculations and are reported in Tab. 1.

The final zero pressure athermal geometry optimisation was then carried out using the converged plane wave basis-set parameters and the generalized-gradient-approximation xc functionals PBE and PBEsol both with and without applying the TS and D2 dispersion corrections. In addition to these optimisations the MBD dispersion correction scheme was used in conjunction with the PBE xc functional. Empirical parameters as used for the various dispersion correction schemes are reported in Section 2.2.

Compound	Input geometry	Cut-off energy (eV)	k-points
CO_2	Simon & Peters, 1980	1300	5 × 5 × 5
C_6H_6	Maynard-Casely et al., 2016	1300	4 × 3 × 4
$MgSO_4$•7H_2O[1]	Fortes et al., 2006	1300	2 × 2 × 4
$CaSO_4$•2H_2O[2]	Comodi et al., 2008	1300	5 × 5 × 5

Tab. 1 Converged basis set parameters and input geometries for all compounds under investigation. [1]the deuterium atoms have been replaced with their light hydrogen counterparts [2]optimisation for $CaSO_4$•2H_2O were carried out using the reduced cell.

The computationally expensive core-valence electron interactions were modelled using ultra soft pseudopotentials (Vanderbilt, 1990). The Broyden-Fletcher–Goldfarb-Shanno method (Pfrommer et al., 1997), allowing for a simultaneous optimisation of the cell parameters and atomic coordinates, was applied to find the geometry corresponding to the lowest total electronic energy. The optimisations were considered converged when the stresses along any component of the Cartesian stress tensor were less than 0.01 GPa.

Additionally, convergence tolerances for the ionic force, ionic displacement and total energy were defined as 0.01 eV/Å, 5×10^{-4} Å and 5×10^{-6} eV/atom, respectively.

2.2. Dispersion corrected DFT

Semi-local exchange correlation functionals such as the PBE and PBEsol xc functionals do not accurately treat long-range forces between atoms arising from correlated electronic fluctuations commonly known as London dispersion forces. By contrast, dispersion forces between two atoms at a distance R decay as $-1/R^6$ (Eisenschitz & London, 1930) semi-local density functional approximations treat the decay exponentially (Ambrosetti et al., 2014).

In order to compensate for this shortcoming, considerable effort has been put into the development of numerous dispersion correction methods. Due to their successful application to a large variety of chemical compounds and being implemented as an off-the-shelf option in many popular quantum chemistry codes (e.g. CASTEP, VASP, Quantum Espresso) we applied the D2 (Grimme, 2006), TS (Tkatchenko & Scheffler, 2009) and MBD (Ambrosetti et al., 2014) correction schemes. For an exhaustive review of other correction schemes the reader is referred to Grimme et al. (2016).

In all of the above mentioned correction schemes the total energy is specified as

$$E_{tot} = E_{KS} + E_{disp} \qquad (1)$$

E_{KS} is obtained from Kohn-Sham DFT as specified in Section 2.1, regardless of the combination the dispersion correction is applied to. However, the various dispersion correction schemes differ in how they retrieve the dispersion energy E_{disp}.

Pairwise-additive dispersion correction method such as the TS and D2 methods rely on the summation over C_{6ij}/R_{ij}^6 terms for pairs of atoms (ij) at a distance R_{ij} using interatomic dispersion correction coefficients C_{6ij}

$$E_{disp} = -s_6 \sum_{i,j} \frac{C_{6ij}}{R_{ij}^6} f_{damp}(R_{ij}, R_{vdw}) \qquad (2)$$

f_{damp} denotes a Fermi-type dampening function which was implemented in both schemes to decrease the dispersion energy to zero at small R_{ij}, thus eliminating the singularity inevitably arising from the $-1/R_{ij}^6$ terms at small interatomic distances.

$$f_{damp}(R_{ij}, R_{vdw}) = \frac{1}{1+e^{-d(\frac{R_{ij}}{s_r R_{vdw}} - 1)}} \qquad (3)$$

The formalism of D2 and TS (eq. 2) is essentially identical, one major difference, however, is the way each of the dispersion corrections derives the atom specific dispersion correction coefficients C_{6i} and van der Waals radii R_{0i}, which are either determined empirically (D2), or derived by from the ground-state electron density and reference values for the free atoms (TS).

TS and D2 are both semi-empirical i.e. for the implementation of dispersion forces empirical parameters have to be specified, which vary between the xc functionals to which the correction is applied. Next to the atom specific dispersion coefficients (C_{6i}) and van-der Waals radii (R_{0i}), a global scaling factor ($s6$), a scaling factor by which the van-der Waals radii are scaled (s_r) and a global factor determining the steepness of the dampening function (d) have to be specified for the D2 correction method. C_{6i} and R_{0i} (already scaled by 1.1) values as reported by Grimme (2006) were used for the PBE + D2 calculations. As for the remaining empirical parameters Grimme (2006) recommended values on the basis of exhaustive benchmarking of 1.10, 0.75 and 20 for the s_6, s_r and d parameter, respectively, to be used for the D2 correction in conjunction with the PBE functional.

For the PBEsol + D2 calculations we followed the approach suggested by Csonka et al. (2008) and fixed the s_6 parameter to unity while rescaling the atom-specific van der Waals radii by 1.42. The values reported for the atom-specific van der Waals radii tabulated in Grimme (2006) were already scaled by 1.10. As pointed out by Tkatchenko & Scheffler (2009), the d parameter relates to the steepness of the dampening term, which

is identical for the D2 and TS correction and was hence fixed to a value of 20, independent of the xc functional and dispersion correction.

The global van der Waals scaling factor s_r was set to optimised functional specific values of 1.06 (Al-Saidi et al., 2012) and 0.94 (Tkatchenko & Scheffler, 2009) for the PBEsol + TS and PBE + TS calculations, respectively.

Next to the pairwise additive schemes, the MBD correction (Ambrosetti et al., 2014), which accounts for the many-body nature of dispersion interactions, was employed in conjunction with the PBE xc functional. The MBD scheme obtains the dispersion energy of a system in a three-step process. First, the atomic polarizabilities are obtained using the TS scheme. Second, the short-range atomic polarizabilities are derived by applying a self-consistent screening on the short-range part of the atomic polarizabilities, which are then used to calculate the long-range correlation energy. The s_r parameter was specified as 0.94 as for PBE + TS and a dimensionless range separating parameter β was set to a value of 0.83.

Many-body dispersion correction schemes from the Grimme family such as the D3 (Grimme et al., 2010) and D4 (Caldeweyher et al., 2017) corrections are not implemented in the CASTEP code as of version 19.1 and hence were not considered in this study. Sample input files for each of the calculations can be found in the supplementary data (Section S2).

2.3. Assessment of agreement with experimental values

The performance in replicating experimentally determined unit-cell dimensions and compression behaviour was evaluated for each of the seven distinct combinations (i.e. PBE, PBE + D2, PBE + TS, PBE + MBD, PBEsol, PBEsol + D2 and PBEsol + TS).

The difference between experimental reference (xEXP) and computationally derived (xDFT) values for each parameter was defined as

$$diff_x = xDFT - xEXP \qquad (4)$$

For this reason, positive and negative $diff_x$ values represent the over and underestimation, respectively, of the DFT values for a given quantity.

For the difference assessment the mean signed difference (MSiD) was calculated

$$MSiD = \frac{1}{N}\sum_i^N diff_{x,i} \quad (5)$$

Despite being useful to identify systematic over or underestimation the MSiD is prone to cancelations (i.e. individual differences will cancel each other out if they are opposite sign). To compensate for this shortcoming, the mean unsigned difference (MUD) was calculated for each category under investigation.

$$MUD = \frac{1}{N}\sum_i^N |diff_{x,i}| \quad (6)$$

2.4. High-pressure calculations, elasticity and acoustic wave propagation

In addition to the zero pressure optimisation, a series of four geometry optimisations at quasi-hydrostatic pressures of 0.5, 1, 1.5 and 2.0 GPa was carried out for each of the seven individual combinations listed in Section 2.1. A third order Birch-Murnaghan Equation of State (BM3-EoS (Birch, 1947)) was fitted to the lattice-parameter data using EOSFIT7-GUI (Gonzalez-Platas et al., 2016). The obtained EoS parameters were evaluated both against each other and against experimentally and computationally derived values from the literature.

The density was interpolated in 0.01 GPa intervals at pressures ranging from 0 to 2.0 GPa using the EoS parameters obtained from fitting the optimized geometries and the experimentally determined literature EoS parameters. Next, we calculated the xDiff, MSiD and MUD with respect to the experimentally determined EoS parameters for each of the seven individual combinations. Moreover, the performance was assessed in terms of relative compressibility. To this end, xDiff, MSiD and MUD were calculated from the V/V_0 data in the above stated pressure intervals and range.

To fully account for each compound's reversible deformation when subjected to any kind of mechanical stress the full elastic tensor was calculated. The elasticity tensor c_{ijkl}, a fourth rank tensor, combines the inducing property, the tensor of mechanical stress σ_{ij}, with the induced property, the strain tensor ε_{kl}

$$\sigma_{ij} = c_{ijkl}\varepsilon_{kl} \qquad (7)$$

The 81 components of the fourth order elastic tensor c_{ijkl} may be reduced to a maximum of 21 independent elastic constants $C_{ij,}$ represented by a symmetric 6×6 matrix. The components of the elastic tensor relate to the elastic constants $C_{ij,}$ following the Voigt notation i.e., $ii = i$ for i= 1, 2, 3 and ij =9 $i - j$ otherwise, yielding

$$\sigma_i = C_{ij}\varepsilon_j \qquad (8)$$

The basic vectors of the Cartesian reference system e_i with i = 1, 2, 3 are related to the crystallographic lattice vectors *a*, *b*, *c* by e_2 // *b**, e_3 // *c* and $e_1 = e_2 \times e_3$ with the * sign denoting the reciprocal lattice vector. For the computation of the elasticity, we chose the combination that scored most highly on the high-pressure benchmarking as well as the PBEsol xc functional to approximate the xc energy. To this end, the structures were initially relaxed using stricter convergence criteria (i.e. $\sigma_{ij} < 0.002$ GPa, maximum ionic force < 0.002 eV/Å, maximum ionic displacement $< 1 \times 10^{-4}$ Å, total energy $< 1 \times 10^{-6}$ eV/atom**)** and each structure was subsequently distorted in discrete increments between limiting strain amplitudes of ±0.003, using the minimum number of strain patterns necessary to retrieve a complete set of elastic constants for the respective crystal systems.

Lattice parameters were fixed, but the internal coordinates were allowed to relax during energy minimisation of the strained structures. The Cartesian stress tensor corresponding to each of the strained structures was then calculated. The analysis of the resulting geometries and computation of the elastic constants was again carried out in Materials Studio. For a more detailed description of the derivation of elastic constants using the stress-strain approach and on the applied strain patterns corresponding to respective crystal systems the reader is referred to Page & Saxe (2002).

The anisotropy of the elasticity was visualised by computing the representation surface of the longitudinal effect of the elastic stiffness (for a definition of the tensor representation surface we refer to Arbeck et al., 2012) using the WinTensor software (Kaminski, 2014).

The computationally determined elastic tensors were compared against experimentally determined literature values by calculating the difference as a percentage with respect to the experimental data for each of the elastic coefficients C_{ij} as well as for acoustic wave velocities in seven crystal directions (i.e., <100>, <010>, <001>, <110>, <011>, <101>, <111>). The transverse and longitudinal polarized shear wave velocities and primary wave velocities were computed using the Christoffel code (Jaeken & Cottenier, 2016) for the

277 computationally and experimentally determined set of elastic constants for each of the crystal directions as
278 stated above. The Christoffel code uses the density and elastic tensor to compute the acoustic wave velocities
279 v of a monochromatic plane wave travelling in direction q for various polarisations p through a crystalline solid
280 according to the Christoffel equation,
281
282 $$(\Gamma_{ik} - \rho v^2 \delta_{ik}) p_k = 0 \qquad (10)$$
283
284 with the Christoffel matrix Γ_{ik} being related to the elastic tensor by
285
286 $$\Gamma_{ik} = c_{ijkl}\, \hat{q}_j \hat{q}_l \qquad (11)$$
287
288 Thus, the solution of the Christoffel equation is an eigenvalue problem, in which one can solve for the
289 eigenvalues ρv^2 and eigenvectors $\boldsymbol{p}$ for a specified crystal direction $\boldsymbol{q}$. By virtue of being an eigenvalue problem
290 of a 3×3 matrix, the determination of wave motion in a crystalline solid yields three solutions, each
291 corresponding to the wave speed of differently polarized plane waves: one primary wave with longitudinal
292 polarisation and two transverse polarised shear waves. The acoustic wave velocities were sampled for various
293 $\boldsymbol{q}$ with the sampling grid defined in the spherical coordinate system as 180 (θ-axis) $\times$ 720 (ϕ-axis) points evenly
294 spaced over half of the unit sphere.
295 The Christoffel matrix for each of the crystal systems under investigation as well as a worked example
296 on how to solve the Christoffel equation for acoustic waves propagating in the direction of the principal axis
297 of an orthorhombic crystal are provided in the supplementary material.
298

3. Results and discussion

3.1. CO_2

CO_2 is one of the most abundant condensed volatiles and has been identified in variety of environments in and outside of the solar system (Minissale et al., 2013). Probably the best known occurrence of solid crystalline CO_2-I (space group $Pa\bar{3}$), colloquially referred to *dry ice*, is in the southern martian polar region where the temperature drop in winter causes the condensation of CO_2 from the martian atmosphere covering the ice shield with a thick layer of solid CO_2 (Byrne & Ingersoll, 2003). Moreover, solid CO_2 is thought to occur on numerous icy objects in the outer solar system (e.g. Johnson, 1996; McCord et al., 1998; Prentice, 1993; Cruikshank et al., 2010; Grundy et al., 2006) and has even been identified in the interstellar medium (D'Hendecourt & Jourdain de Muizon, 1989).

By virtue of exhibiting cubic symmetry the CO_2 crystal lattice may be described by a single cell parameter being inversely proportional to density. For this reason, the zero pressure athermal performance was not assessed and will be discussed separately with the high-pressure density profiles.

Despite being subject of numerous studies focussing on the exploration of its thermoelastic properties, there are just three studies (i.e. Manzhelii et al., 1971; Powell et al., 1972; Stevenson, 1957) reporting the bulk modulus of CO_2 in the below-room temperature region. Out of these three studies the compressibility reported by Stevenson (1957) is in doubt (Olinger, 1982), leaving compressive parameters as obtained by Manzhelii et al. (1971) from speed of sound measurements in the 80 – 190 K range and extrapolated to athermal conditions, as well as the full elastic tensor determined by Powell et al. (1972) at 95 K by means of inelastic Neutron scattering, as the only reliable experimentally determined reference data in the below room temperature region. Giordano et al. (2010) experimentally determined the compressibility along various high-tempeature isotherms and combined these data with literature compression data in a Mie-Grüneisen-Debye (MGD) model. The athermal bulk modulus and unit-cell volume as obtained from the MGD fit were in good agreement with the

experimentally determined reference data, granting the validity of the model, which was therefore chosen for the performance evaluation of the computed density-pressure profiles.

The density is systematically overestimated, regardless of the functional/dispersion correction applied (Tab. 2). PBE + D2 demonstrates the best performance, overestimating the zero pressure athermal volume reported by Giordano et al., 2010 by only 5.4 %. The PBEsol + D2 ranks second, followed by PBEsol + TS, PBE + MBD, PBE + TS, PBEsol, and lastly PBE being the worst performing approach overestimating the cell volume by 28.8 %.

The PBEsol + D2 agrees best with the reference athermal density-pressure profile, closely followed by the PBEsol + TS and PBE + D2, as the top performing combination in the zero-pressure benchmarking category, just on the third place (Fig. 1). When assessing the high-pressure performance in terms of relative compressibility, however, it is apparent that the seemingly excellent performance of the dispersion corrected PBEsol approaches is due to a cancellation of errors, stemming from the overestimation of the cell volume and underestimation of the materials stiffness. In detail, PBEsol + D2 and PBEsol + TS substantially underestimate the material's stiffness ranking ex aequo on 4th rank in the relative compressibility benchmarking category, whereas the top performing combination, PBE + D2, accurately models the relative compression with a MUD of just 1.0 % and therefore, may be considered as the top performing combination in the high-pressure category.

As a general trend, even the worst performing dispersion corrected calculations yield a substantial improvement over their non-dispersion corrected counterparts (Fig. 1). It is further noteworthy, that although performing poorly when evaluated against the athermal reference data, the compressibility obtained by the PBE and PBEsol xc functional demonstrates excellent performance when compared to the experimental room temperature pressure profile (Fig. 1) determined by Giordano et al. (2010).

When comparing room temperature compression data for solid CO_2 (Tab. 2) it should be taken into account that the non-existence of solid CO_2 at standard conditions renders it impossible to experimentally determine V_0 at room temperature, with both K and K' being sensitive to changes in V_0 (Giordano et al., 2010). Comparing their experimental room temperature compression data to earlier studies published by Olinger (1982) and Liu et al. (1984), Giordano et al. (2010) conclude that the data are in good agreement, but the standard deviations in earlier studies are larger due to poor coverage in the low-pressure region and larger scatter of data-points.

V_0 (Å^3)	K (GPa)	K'	T (K)	EoS	Method	Source
220.81(70)	2.85(15)	7.40(40)	0	BM-3EOS	DFT: PBE	This study
180.73(13)	7.76(20)	9.26(40)	0	BM-3EOS	DFT: PBE+D2	This study
195.58(28)	6.57(23)	5.80(35)	0	BM-3EOS	DFT: PBE+TS	This study
190.54(28)	6.70(31)	5.75(58)	0	BM-3EOS	DFT: PBE+MBD	This study
195.88(1.43)	2.72(47)	11.18(1.82)	0	BM-3EOS	DFT: PBEsol	This study
183.99(41)	4.68(27)	8.87(62)	0	BM-3EOS	DFT: PBEsol+D2	This study
184.60(17)	4.69(11)	8.64(26)	0	BM-3EOS	DFT: PBEsol+TS	This study
157.4(3)	16.5(4)	6.8(1)	0	BM3-EOS	MP2	Li et al., 2013
147.48	16.6	N/S	0	N/S	DFT:LDA	Gracia et al., 2004
212.2	3.21	8.10	0	BM-3EOS	DFT: PBE	Bonev et al., 2003
171.40(44)	10.4(4)	6.8(4)	0	MGD	MGD-Model	Giordano et al., 2010
171.64	8	N/A	0*	N/A	Speed of sound	Manzhelii et al., 1971
N/S	8.67	N/A	95	N/A	Inelastic neutron scattering	Powell et al., 1972
201.98^F	3.0^F	8.55^F	295	N/A	MGD-Model	Giordano et al., 2010
204(12)	2(1)	9(1)	296	Vinet	WC-anvil cell	Olinger, 1982**
208.6(1.3)	2.93(10)	7.8	296(2)	BM3-EOS	DAC	Liu et al., 1984
N/S	12.4	N/S	RT	N/S	DAC	Yoo et al., 1999

Tab. 2 Computationally derived athermal bulk moduli of CO_2 from this study and the literature compared to the experimental values for CO_2. Bulk moduli from speed of sound measurements and inelastic neutron scattering are Voigt-Reuss-Hill averages whereas the ones derived from isothermal compression series are adiabatic. *****Speed of sound measured between 88 – 190 K and extrapolated to 0 K. ****** EoS parameters as reanalysed and stated by Giordano et al. (2010). RT denotes that the data was acquired at room temperature. N/S denotes that this information is not stated by these authors. ^{F} indicates that the parameter was fixed during the fitting procedure.

Comparing the performance of this studies' best performing combination, PBE + D2, compressive parameters (5.4 %, –25.4 % and 36.2 % difference to the experimental reference values on V_0, K and K' respectively) to earlier DFT studies by Bonev et al. (2003) (i.e. PBE, 23.0 %, –69.1 %, 19.1 % difference to the experimental reference values on V_0, K and K', respectively) and Gracia et al. (2004) (i.e. LDA, – 14.0 % and 59.6 % difference to the experimental reference values on V_0 and K) reinforces the improved accuracy associated with the implementation of dispersion correction schemes into Kohn-Sham DFT calculations.

Regarding further gain of accuracy by increasing the level of theory, we want to point out that the Post-Hartree-Fock calculations of the second order Møller-Plesset perturbation (MP2) theory type by Li et al. (2013) substantially underestimate the volume and overestimate the stiffness[1]. It is a well-studied phenomenon that MP2 performs badly for dispersion dominated systems (Cybulski & Lytle, 2007), thus explaining the higher accuracy achieved in our calculations.

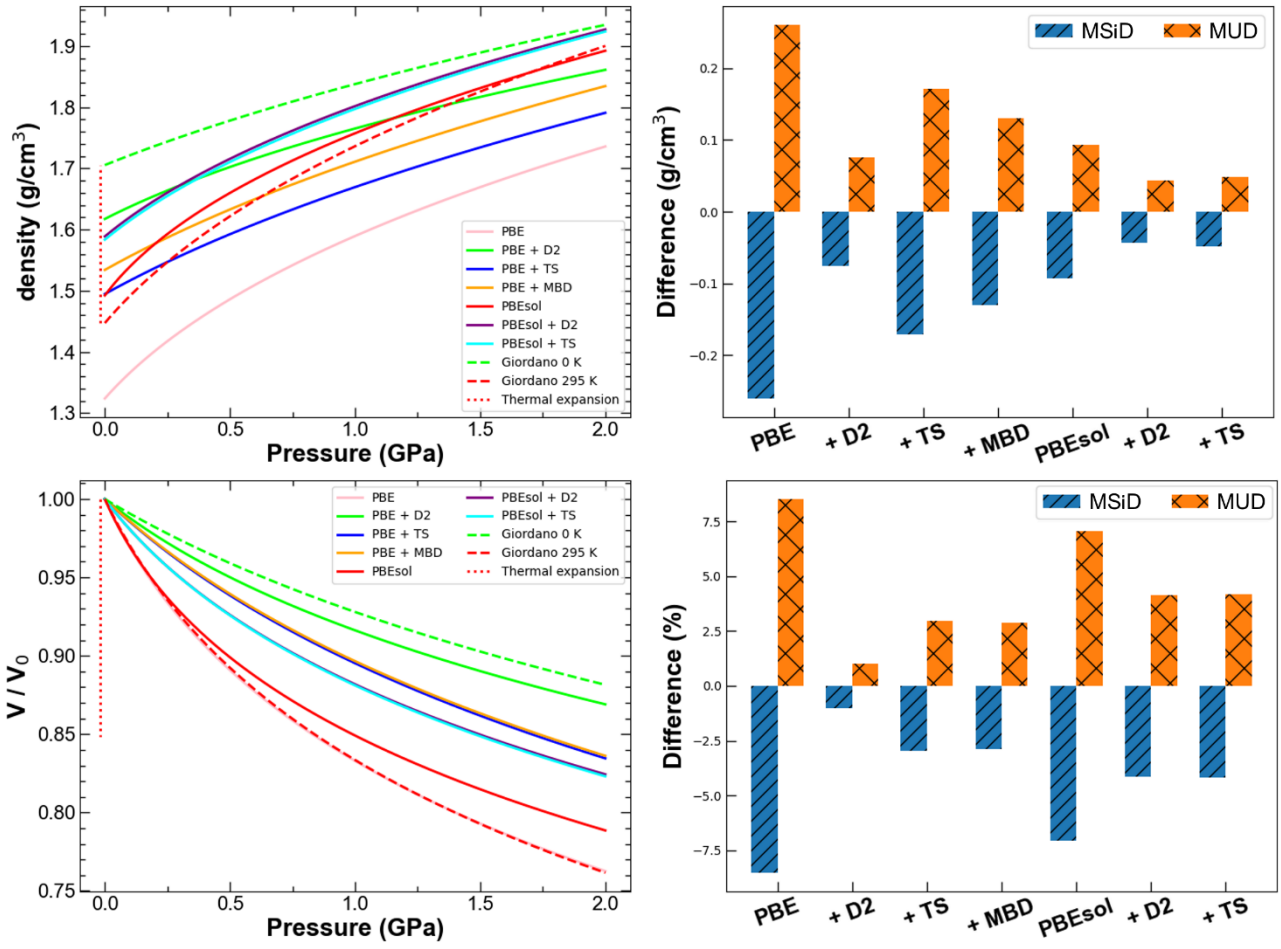

Fig. 1 Density profiles and relative compressibility of CO_2, and their performance assessed in terms of MSiD and MUD. While the dispersion corrected PBEsol approaches yield a low average error on the density, they fail to reproduce the relative compressibility. The dispersion corrected PBE functionals, however, reveal excellent performance for both the density and relative compressibility.

[1] −8.2 %, 58.6 % and 0.0 % difference to the experimental reference values on V_0, K and K' respectively, compressive parameters by digitizing the volume pressure plot and subsequent equation of state fitting

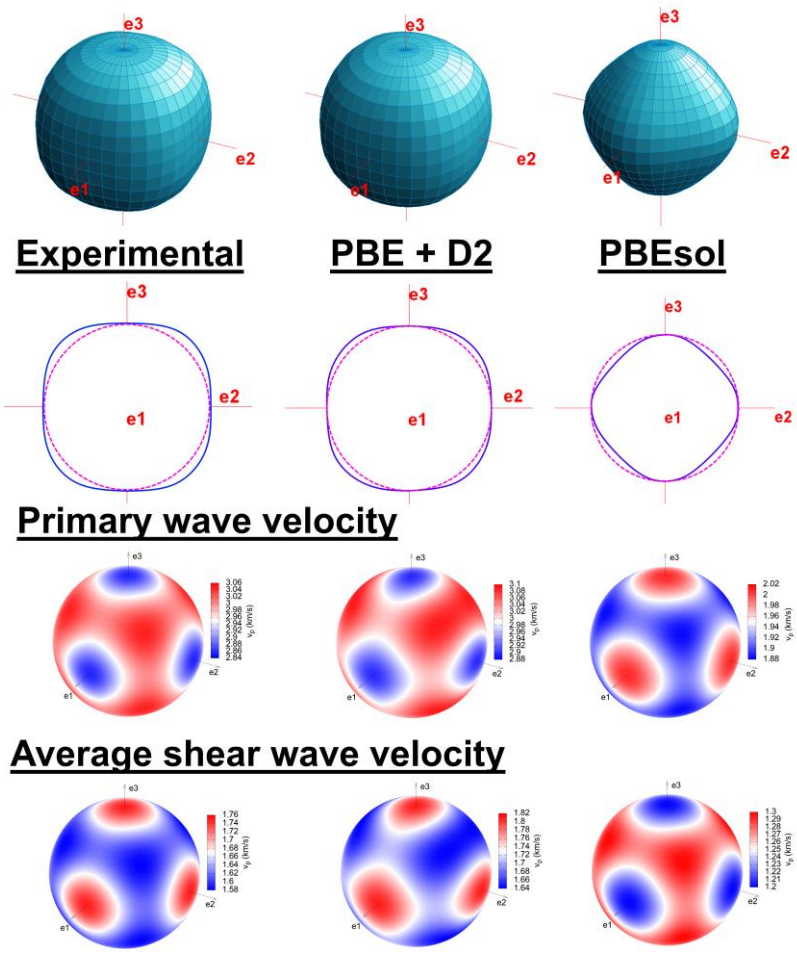

Fig. 2 Representation surfaces of the longitudinal effect of the elastic stiffness of CO_2 clearly demonstrate that PBE + D2 excellently reproduces the materials elasticity, whereas PBEsol fails to do so. From comparing cross-sections along the principal tensor axis (blue) with a circle whose radius corresponds to the magnitude of maximum stiffness (magenta), it becomes apparent that while for the PBE + D2 and experimental tensor the direction of maximum and minimum compressibility are <110> and <100> respectively: this is inverted for the PBEsol derived tensor. Naturally, this inversion is also reflected in the seismic wave velocities.

The elastic constants of CO_2 were computed using the PBEsol and PBE + D2 combinations and then benchmarked against the experimental reference constants reported by Powell et al. (1972) at 95 K. PBE + D2 is in excellent agreement with the reference data, differing by merely 0.0 % (C_{11}), −14.7 (C_{12}) and 2.5 % (C_{44}), whereas PBEsol largely fails to model the elastic anisotropy underestimating the elastic constants by 55.6 to 90 % (Tab. 3). PBEsol further fails to accurately model the directions of minimum and maximum stiffness (Fig. 2). Both, PBE + D2 and the experimental data show that the <110> and <100> are directions of maximum and minimum stiffness respectively, whereas PBEsol draws an inverted picture with the stiffness reaching a maximum in <100> and a minimum in <110>. This failure to accurately model the elastic anisotropy, clearly, results in an inversion of the maximum and minimum directions of seismic wave velocities as compared to the

experimental reference data (Fig. 2). Regarding the absolute accuracy of the computed seismic wave velocities, we note that the agreement between PBE + D2 and the experimental data is striking with a MUD of 1.36 % and 3.88 % for the P and S waves, respectively. PBEsol completely fails to reproduce the seismic wave velocities underestimating the P and S wave velocities by 33.68 % and 25.15 %, respectively.

C_{ij}	Exp	PBE + D2	Diff %	PBEsol	Diff %
C_{11}	13.60(6)	13.60(14)	0.0	6.04(18)	−55.6
C_{12}	6.2(1)	5.29(31)	−14.7	0.62(13)	−90.0
C_{44}	5.10(3)	5.23(7)	2.5	2.16(29)	−57.6
K	8.67	8.02	−7.5	2.43	−72.0
G	4.54	4.82	6.2	2.36	−48.0
T	95	0		0	

Tab. 3 Computed elastic constants of CO_2 evaluated against the experimental coefficients as reported by Powell et al. (1972). Bulk and shear moduli were computed using the Christoffel code whereby the density corresponding to 95 K was interpolated from the 90 and 100 K values as reported by Manzhelli et al. (1971). Temperatures are in K, all other values in GPa. Diff % gives the deviation of the preceding value from the corresponding experimental value in %.

3.2. C_6H_6

Polycyclic aromatic hydrocarbons are abundant in the universe, contributing an estimated 20 – 30 % to the galactic infrared radiation (Peeters, 2011), and serve as indicator to determine star formation rates (Calzetti, 2011), unarguably a key parameter in understanding a galaxy's formation and evolution. From a topological perspective, polycyclic aromatic hydrocarbons may be described in a simplified manner as fused benzene rings.

Unsurprisingly, considering the cosmic abundance of polycyclic aromatic hydrocarbons, benzene (C_6H_6; space group: *Pbca*) as their fundamental building block has been specifically identified in a large variety of extra-terrestrial settings such as carbonaceous meteorites (Mullie & Reisse, 1987), protoplanetary nebula CRL618 (Cernicharo et al., 2001), and in Titan's atmosphere (Vinatier et al., 2017). The latter occurrence appears to be of special interest from a planetary science perspective, since Vuitton et al. (2008) suggested that the atmospheric benzene, among other aromatics, could condense as it diffuses downwards in Titan's atmosphere covering the surface with a layer of solid benzene. Moreover, Malaska & Hodyss (2014) studied the solubility of hydrocarbons in simulated Titan lake and concluded that Titan's lakes might saturate in benzene from direct airfall over geological timescales and may form hydrocarbon deposits in a similar fashion as terrestrial evaporitic deposits. Seismology has demonstrated to be a powerful (Cornelius & Castagna, 2017), albeit notoriously difficult method (Jones & Davison, 2014), in order to explore terrestrial evaporite deposits and may also be able to cast light on the mineralogical phase assemblage of these putative hydrocarbon deposits, subject to the condition that the elastic wave velocities of benzene and other candidate materials are accurately known.

The zero pressure athermal unit-cell dimensions were benchmarked against the experimental values determined by Fortes & Capelli (2018) at 10 K by means of high-resolution neutron powder diffraction (Fig. 3). PBE and PBEsol both overestimate the cell volume, whereas the implementation of dispersion corrections results in an underestimation. Again, all dispersion corrected combinations yield a substantial improvement

over their non-dispersion corrected counterparts. For PBE the implementation of a dispersion correction reduced the average absolute difference on the lattice parameters by 63 %, 88%, 98% for the PBE + D2, PBE + TS and PBE + MBD, respectively.

As for the PBEsol based calculations, implementation of a dispersion corrections improves the performance and reduces the average absolute difference on the lattice parameters by 49 % and 51 % for the PBEsol + D2 and PBEsol + TS, respectively. Overall, the PBE + MBD is the best performing combination with an MUD of merely 0.014 Å (Fig. 3).

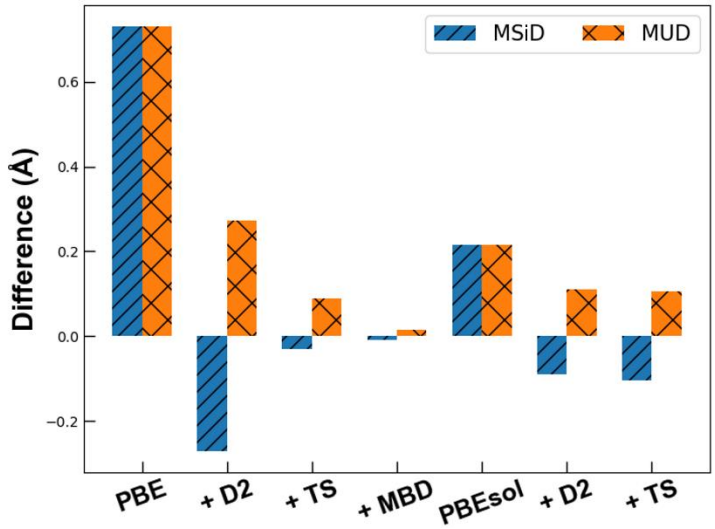

Fig. 3 MSiD (blue) and MUD (orange) of the DFT lattice vectors of C_6H_6 benchmarked against the Fortes & Capelli (2018) values determined at 10 K.

First exploration of the high-pressure behaviour of benzene dates back to pioneering work of Ferche (1891), Heydweiller (1897), Tammann (1903), Meyer (1910), and Bridgman (1914). More recently, pressure-volume data for benzene were reported by Figuière et al. (1978) and Katrusiak et al. (2010). After digitizing and fitting the pressure-volume data reported in Figuière et al. (1978) it was evident that values of ~0.5 as obtained for *K'* are unrealistically low for such a soft solid as benzene. Fitting of a BM3-EOS to the Katrusiak et al., 2010 data yielded much more realistic EoS parameters V_0 = 522.43 Å^3, K = 2.32 GPa, K' = 9.85 which was used as experimental reference data for our benchmarking purposes as presented in Tab. 4.

One drawback of benchmarking against the Katrusiak et al. (2010) data is that the compressibility was determined along the 295 K isotherm. Therefore, the effect of temperature will be discussed accordingly in the performance evaluation.

V_0 (Å^3)	K (GPa)	K'	T (K)	EOS	Method	Source
610.60(58)	1.29(2)	10.83(13)	0	BM-3EOS	DFT: PBE	This study
417.21(27)	10.71(31)	10.46(57)	0	BM-3EOS	DFT: PBE+D2	This study
461.05(10)	9.21(7)	7.12(10)	0	BM-3EOS	DFT: PBE+TS	This study
462.15(25)	7.45(12)	7.97(22)	0	BM-3EOS	DFT: PBE+MBD	This study
502.63(76)	2.51(9)	12.73(44)	0	BM-3EOS	DFT: PBEsol	This study
449.20(31)	8.82(18)	5.22(23)	0	BM-3EOS	DFT: PBEsol+D2	This study
446.02(24)	6.97(11)	7.85(20)	0	BM-3EOS	DFT: PBEsol+TS	This study
484.89	8.2 (1)	6.8 (1)	0	Vinet	DFT:optPBE–vdW	Litasov et al., 2019
N/A	4.60	N/A	250	N/A	Speed of sound	Heseltine et al., 1964
N/A	5.85	N/A	170	N/A	Speed of sound	Heseltine et al., 1964
N/A	6.30	N/A	138	N/A	Speed of sound	Walmsley, 1968
522.43(88)	2.32(10)	9.85(43)	RT	BM-3EOS	Piston + DAC	Katrusiak et al., 2010

Tab. 4 Computationally derived athermal bulk moduli of C_6H_6 from this study and the literature compared to the experimental values. Bulk moduli from speed of sound measurements are Voigt-Reuss-Hill averages whereas the ones derived from isothermal compression series are adiabatic.

The PBEsol functional comes out on top of both the density profile and relative compressibility benchmark (Fig. 4), which we attribute to a cancellation of the underestimation of the density and stiffness, paired with the benchmarking being carried out against room temperature data. PBE performs poorly in modelling the density profile, but came second in the relative compressibility benchmarking category, once more validating that non-dispersion corrected functional perform very well for room temperature data. We expect the bulk modulus to substantially increase approaching the athermal limit, which is supported by low-temperature bulk moduli of 4.60, 5.85 and 6.28 GPa as obtained at 250, 170 and 138 K in speed of sound measurements (Heseltine et al., 1964; Walmsley, 1968). Comparing the PBE and PBEsol derived bulk moduli of 1.29(2) GPa and 2.51(9) GPa, respectively, to this low-temperature studies it is apparent that both functionals fail to accurately reproduce the stiffness in the low-temperature region. The dispersion corrected PBE yield more realistic bulk moduli ranging from 7.45 to 10.71 GPa. A bulk modulus of 8.2 GPa as derived by Litasov et al., 2019 using the optPBE-vdW approach compares very well to both our dispersion corrected and the experimental low-temperature values.

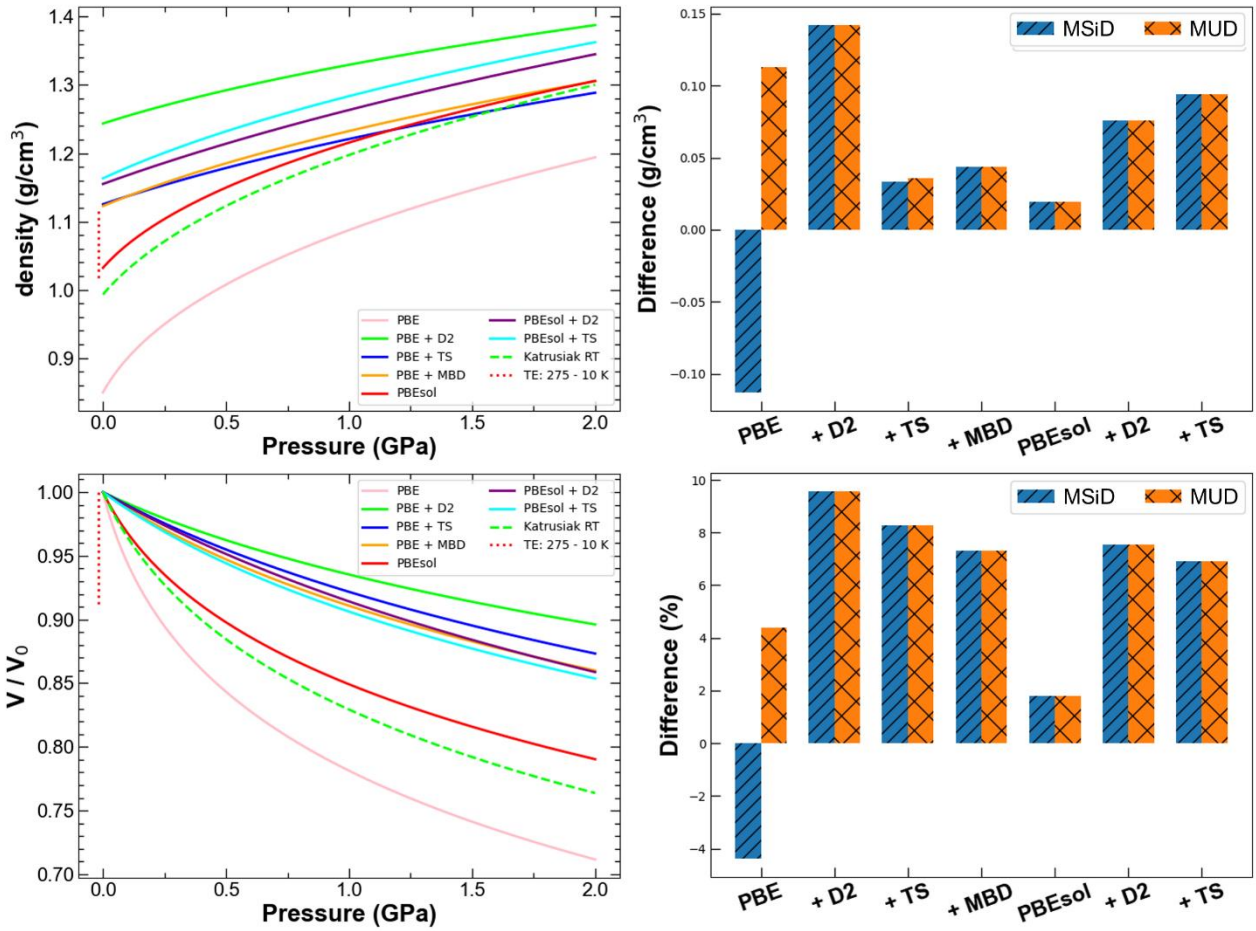

Fig. 4 Density profiles and relative compressibility of C_6H_6 and their performance assessed in terms of MSiD and MUD. We note the excellent agreement between the 10 K density and the PBE + TS and PBE + MBD approaches. Clearly, this is not reflected in the relative compressibility likely due to the benchmarking being carried out against room temperature data.

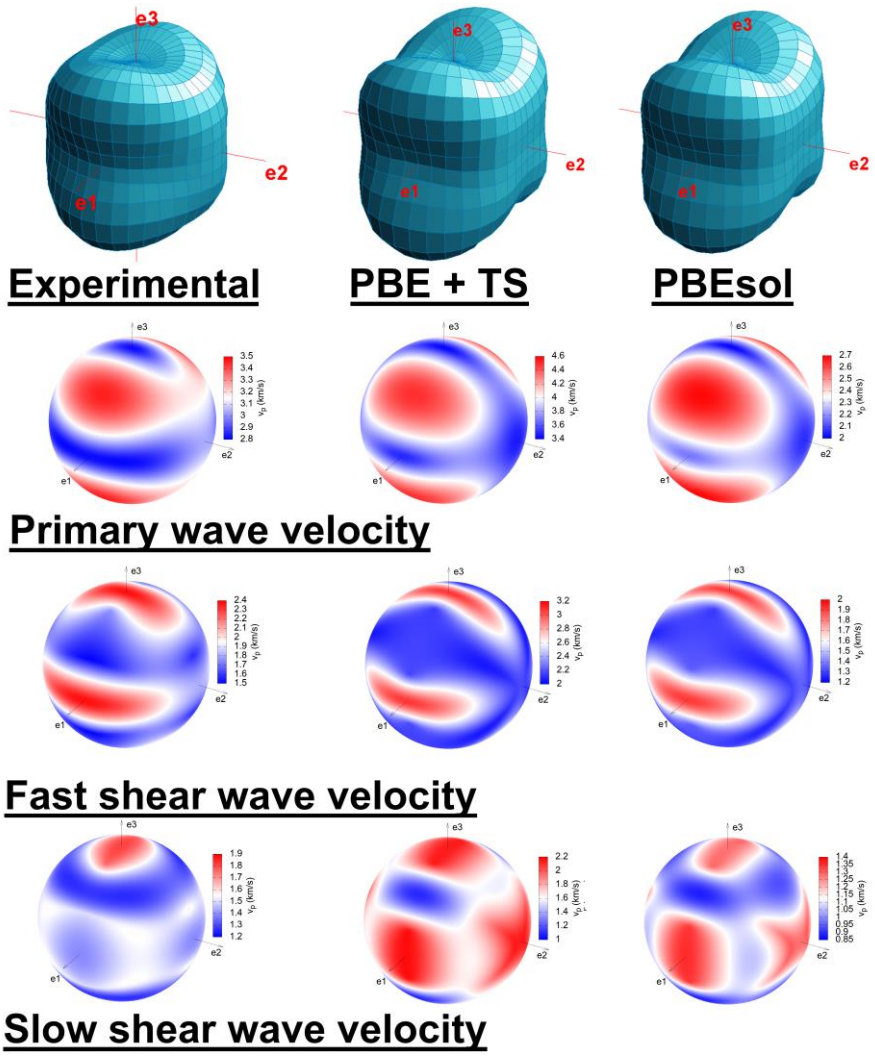

Fig. 5 Representation surfaces of the longitudinal effect of the elastic stiffness of C_6H_6 clearly demonstrates that both the PBEsol and PBE+TS approximate the experimental values (Walmsley, 1968) reasonably well. The anisotropy, however, is not completely accounted for, which is most pronounced in the slow shear wave velocities.

C_{ij}	Exp*	PBEsol	Diff %	PBE + TS	Diff %	Exp**	Exp***
C_{11}	8.61	4.84(32)	−43.8	13.71(90)	59.2	6.14	8.01
C_{22}	10.01	4.39(33)	−56.1	13.48(1.52)	34.7	6.56	9.26
C_{33}	8.63	4.16(45)	−51.8	13.12(46)	52.0	5.83	7.88
C_{12}	4.15	2.29(47)	−44.8	7.68(72)	85.1	3.52	3.85
C_{13}	5.10	2.87(29)	−43.7	10.73(53)	110.4	4.01	4.80
C_{23}	5.38	2.46(53)	−54.3	7.81(71)	45.2	3.90	5.08
C_{44}	3.56	1.68(25)	−52.8	5.14(38)	44.4	1.97	3.18
C_{55}	6.13	3.77(12)	−38.5	10.61(37)	73.1	3.78	5.53
C_{66}	2.10	1.89(29)	−10.0	5.31(54)	152.9	1.53	1.95
Mean			-44		73		
K	6.28	3.17	−49.5	10.26	63.4	4.60	5.85
G	3.20	1.63	−48.8	4.22	31.9	1.93	2.89
T	138	0		0		250	170

Tab. 5 Computed elastic constants of C_6H_6 evaluated against the experimental coefficients as reported by *Walmsley, 1968 at 138 K. Moreover, the elasticity reported by Heseltine et al., 1964 at 250 K (**) and 170 K (***) is reported for comparison. Bulk and shear moduli were computed using the Christoffel code whereby the densities corresponding to the experimental temperatures of 138 K, 170 K and 250 K were either directly calculated from the experimentally determined unit-cell volume (i.e. 250 K; Fortes & Capelli (2018)) or, if no volume data corresponding to the temperature was available (i.e.138 K and 170 K), interpolated from the two closest data-points as listed in Fortes &Capelli (2018). Temperatures are in K, all other values in GPa. Diff % gives the deviation of the preceding value from the corresponding experimental value in %.

The elastic constants of C_6H_6 were computed using the PBEsol and PBE + TS approaches and then benchmarked against the experimental reference determined by Walmsley (1968) at 138 K (Tab. 5). The stiffness is systematically overestimated by the PBE + TS functional and underestimated by the PBEsol functional. At first sight, the longitudinal effect of the elastic stiffness appears well approximated by both combinations with the maximum direction being along <101> and the local minima parallel to the principal tensor axes. Looking more closely, however, subtle discrepancies become apparent. The experimental data displays an elastic anisotropy along the principal axes with $C_{22} > C_{11} = C_{33}$ resulting in the P waves travelling faster along <010> than <100> and <010>. The DFT-derived tensors, however, yield identical values within the limits of errors for respective directions and hence fail to reproduce the anisotropy along the principal tensor axes e_i.

The experimental data further reveals slow shear waves propagating in the <010> and <100> direction, which are both solely dependent on C_{66} and hence constrained to be equivalent in an orthorhombic crystal by the Christoffel equation, being substantially slower than those travelling in the C_{44} dependent <001> direction (Fig. 5). The DFT calculations, again, failed to reproduce this effect and yielded nearly identical slow shear wave velocities for the principal directions stemming from similar C_{44}/C_{66} ratios of 0.88 and 0.95. These are much lower than a value of 1.7 corresponding to the C_{44}/C_{66} ratio of the experimentally determined elastic constants. PBE + TS and PBEsol bracket the experimental values over- and underestimating the elastic constants by 73 % and −44 %, respectively. Naturally, this is also reflected in the seismic wave velocities differing by 23.95 % (P, PBE + TS), 24.71 % (S, PBE + TS) −25.6 % (P, PBEsol), and −21.6 % (S, PBEsol) from the literature reference data. Clearly, benchmarking against lower temperature data, which to our knowledge are not available, would increase and decrease the performance of PBE + TS and PBEsol, respectively.

In general, the elasticity is well approximated, albeit neither approach fully accounts for the elastic anisotropy. Absolute errors on the seismic wave velocities, obtained with either of the functionals, are far from experimental accuracy and hence not suitable for use in a seismic velocities reference data-base.

3.3. $MgSO_4 \cdot 7H_2O$

Remote sensing of the surface of the outer three Galilean moons (i.e. Europa, Ganymede and Callisto) by the *Galileo* near-infrared mapping spectrometer (McCord et al., 1998, 2001) indicates that epsomite ($MgSO_4 \cdot 7H_2O$; space group: $P2_12_12_1$), among other hydrated minerals, is a promising candidate to partially constitute the non-icy material identified on their surface. As for the origin of $MgSO_4 \cdot 7H_2O$ on the European surface both endogenic (i.e. from brine crystallisation; McCord et al., 1998) and exogenic (i.e. via the radiolysis of endogenic $MgCl_2$ in conjunction with sulfur ion bombardment from neighbouring Io; Brown & Hand, 2013) processes are being discussed.

The compressibility of epsomite-type $MgSO_4 \cdot 7D_2O$ was determined by Fortes et al. (2006) by means of neutron powder diffraction in the temperature range 50-290 K and up to 0.5 GPa. Gromnitskaya et al. (2013) explored the bulk compressibility of $MgSO_4 \cdot 7D_2O$ and $MgSO_4 \cdot 7H_2O$ via speed of sound measurements and demonstrated that the effect of deuteration upon the elastic properties of the isotopologues is small (i.e., hydrogenated K = 18.8 GPa, deuterated K = 21.6 GPa). For this reason, we suggest that the equation of state as determined by Fortes et al. (2006) along the 50 K isotherm approximates the compressibility of $MgSO_4 \cdot 7H_2O$ close to athermal conditions reasonably well, and therefore chose these data as an experimental reference for our benchmarking purposes.

After benchmarking the DFT derived unit-cell dimensions with respect to the values experimentally determined by Fortes et al. (2006) at a temperature of 2 K (atmospheric pressure), it was apparent that the PBE optimisation yielded an overestimation of all lattice parameters and consequently the cell volume, whereas the other combinations underestimate this quantity (Fig. 6). The PBE xc functional, in conjunction with the pairwise additive (i.e. D2 and TS) correction schemes, as well as the many body dispersion correction, agree best with the experimentally determined crystal structure. The excellent performance of PBE + TS and PBE + MBD appears to at least partially stem from a cancellation of an overestimation of the *a* and underestimation of *b* lattice parameter, which is reflected in an excellent MSiD but substantially poorer MUD (Fig. 6). The

geometries obtained by the non-dispersion corrected PBEsol and the dispersion corrected PBE approaches agree excellently with the experimental reference data (i.e. MUD ranging from 0.039 to 0.050 Å), whereas the non-dispersion corrected PBE and the dispersion corrected PBEsol combinations yield an approximately three fold higher average error (i.e. MUD 0.122 - 0.155 Å) on the individual lattice parameters and largely over- and underestimated the cell volume, respectively (Fig. 6).

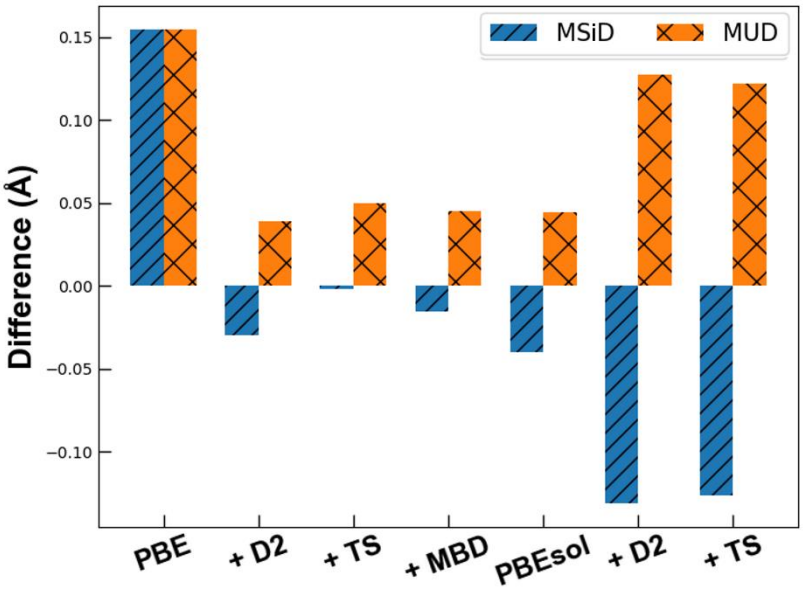

Fig. 6 MSiD (blue) and MUD(orange) of the DFT lattice vectors of $MgSO_4 \cdot 7H_2O$ benchmarked against the values determined at 2 K (Fortes et al., 2006) for the deuterated isotopologue.

The performance in replicating the density's pressure dependency was evaluated against the along the 50 K isotherm experimentally determined EoS parameters as reported by Fortes et al. (2006) (Fig. 7, Tab. 6). The combinations that came out on top of the zero pressure athermal benchmarking category, i.e. PBE + TS, PBE + D2 and PBEsol, also demonstrated superior performance in approximating the reference density profile. The PBE functional reveals almost identical performance as the PBE + TS approach in the relative compressibility (V/V_0) category, which can at least be partially attributed to a bias of the compressive parameters as reported by Fortes et al. (2006) towards this functional, since they fixed *K'* to 5.3, a value they have determined by high-pressure geometry optimisations using the PW91 functional. It is well known, that PW91 and PBE produce essentially identical bulk moduli (Mattsson et al., 2006), an observation that is also reflected in our results, with the difference between this studies' PBE and the Fortes et al. (2006) PW91 merely

being 0.4 %, 6 % and 4 % on V_0, K and K', respectively. Furthermore, we point out that the PBE xc functional is the worst performing functional in modelling the experimental density profile (Fig. 7), hence the excellent performance in modelling the relative compressibility likely originates from aforementioned bias and a cancellation of the density and compressibility underestimation. The performance of the PBE + TS in replicating the experimental density profile is excellent, with the MUD just being 0.003 g/cm^3, and was therefore chosen for the computation of the elastic constants.

V_0 (Å^3)	K (GPa)	K'	T (K)	EoS	Method	Source
1002.23(28)	24.13(45)	5.94(52)	0	BM-3EOS	DFT: PBE	This study
951.09(10)	29.00(24)	3.60(24)	0	BM-3EOS	DFT: PBE + D2	This study
956.94(7)	29.13(15)	3.80(15	0	BM-3EOS	DFT: PBE + TS	This study
955.05(1.51)	29.25(3.5)	3.15(3.42)	0	BM-3EOS	DFT: PBE + MBD	This study
947.00(33)	29.60(77)	3.46(76)	0	BM-3EOS	DFT: PBEsol	This study
921.59(0.48)	31.02(1.38)	6.00(1.54)	0	BM-3EOS	DFT: PBEsol + D2	This study
922.69(19)	33.26(56)	3.23(55)	0	BM-3EOS	DFT: PBEsol + TS	This study
998.14(51)	23.2(2)	5.3(2)	0	BM-3EOS	DFT: PW91	Fortes et al., 2006
961.17(7)^D	25.0(2)	5.3^F	50	BM-3EOS	NPD+PE-Press	Fortes et al., 2006
973.80(7)	21.5(1)	5.3^F	295	BM-3EOS	NPD+PE-Press	Fortes et al., 2006
N/S	21.6	5.0	RT	N/S	Lever-Piezometer	Bridgman, 1949
N/A	21.6	5.2	295	N/A	Speed of sound	Gromnitskaya et al., 2013
N/A	18.8^D	4.2	295	N/A	Speed of sound	Gromnitskaya et al., 2013
N/A	22.2(7)	N/A	RT	N/A	Speed of sound	Alexandrov et al., 1963
N/A	28.99	N/A	RT	N/A	Speed of sound	Voronkov, 1958
N/A	43.5	N/A	RT	N/A	Speed of sound	Sundara Rao, 1950

Tab. 6 Computationally derived athermal bulk moduli of $MgSO_4 \cdot 7H_2O$ from this study and the literature compared to the experimental values. Bulk moduli from speed of sound measurements are Voigt-Reuss-Hill averages whereas the ones derived from isothermal compression series are adiabatic. N/S denotes that this information is not stated by these authors. ^{F}indicates that the parameter was fixed during the fitting procedure. ^{D}deuterated isotopologue. RT denotes that the data was acquired at room temperature.

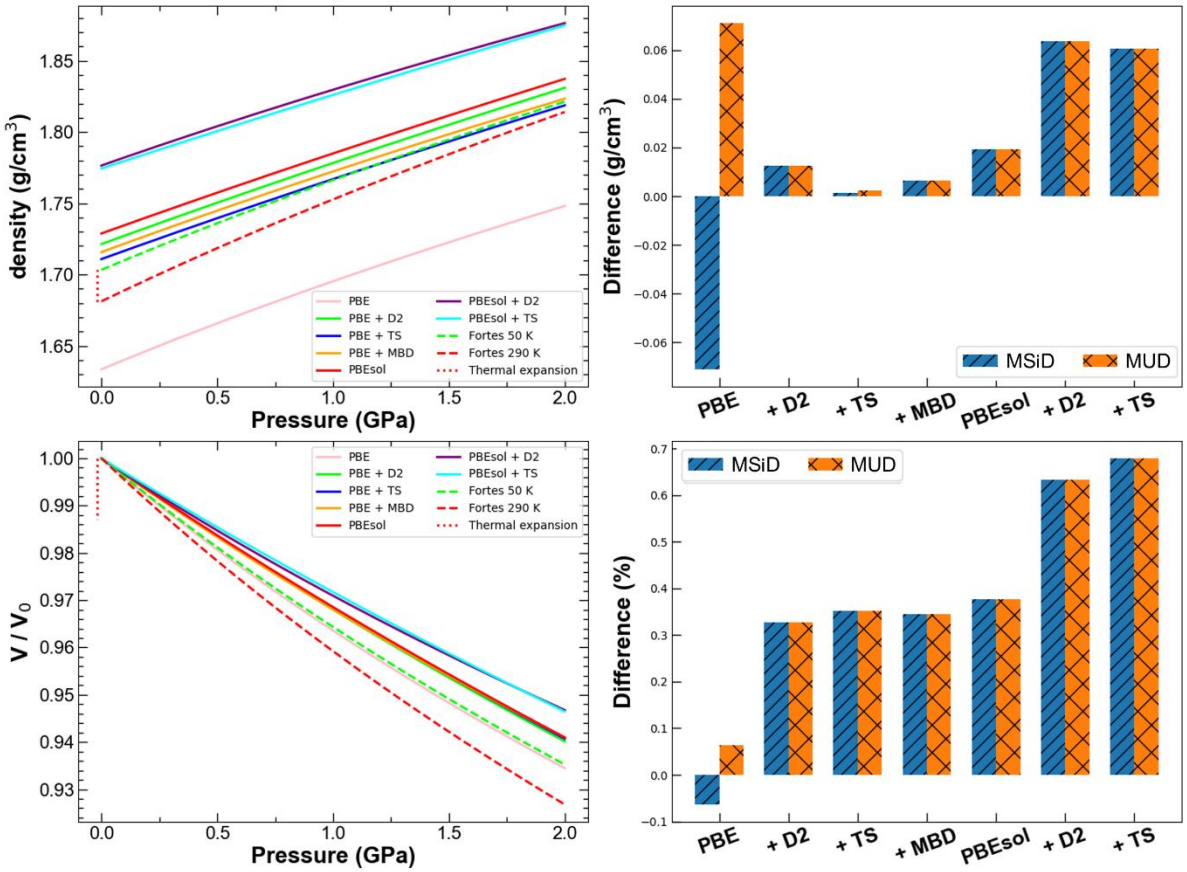

548

549 **Fig. 7** Density profiles and relative compressibility of $MgSO_4 \cdot 7H_2O$ and their performance assessed in terms of MSiD and MUD. We note the
550 excellent performance of the PBE +TS approach in replicating the experimental density pressure profile.

551 To our knowledge, three studies (i.e. Alexandrov et al, 1963; Sundara Rao, 1950; Voronkov, 1958)
552 have experimentally determined a complete set of the elastic constants of epsomite. Fortes et al. (2006)
553 evaluated the axial compressibility as determined by means of high-pressure neutron diffraction against values
554 derived from the elastic tensors, reported in the aforementioned studies, and concluded that the elastic tensor
555 values determined by Sundara Rao (1950) and Voronkov (1958) were in doubt, whereas the elastic constants
556 reported by Alexandrov et al. (1963) revealed satisfactory agreement. For this reason, and due to the lack of
557 reference elastic constants experimentally determined at low-temperatures, values as reported by Alexandrov
558 et al. (1963) were selected for benchmarking purposes. The effect of temperature on epsomite's stiffness
559 (Fortes et al., 2006) is less dramatic than in CO_2 or C_6H_6, but still pronounced and will hence be discussed
560 accordingly.

561

C_{ij}	Exp	PBEsol	Diff %	PBE + TS	Diff %
C_{11}	32.5(7)	54.84(1.30)	68.7	50.15(72)	54.3
C_{22}	28.8(6)	41.18(6)	43.0	40.83(72)	41.8
C_{33}	31.5(6)	46.27(1.23)	46.9	44.77(1.76)	42.1
C_{12}	17.4(17)	20.31(25)	16.7	19.68(22)	13.1
C_{13}	18.2(18)	24.26(61)	33.3	24.6(59)	35.2
C_{23}	18.2(18)	20.63(30)	13.4	20.97(24)	15.2
C_{44}	7.8(2)	14.11(42)	80.9	13.9(29)	78.2
C_{55}	15.6(3)	21.24(8)	36.2	21.56(17)	38.2
C_{66}	9.0(2)	13.35(28)	48.3	12.97(38)	44.1
Mean			43.0		40.2
K	22.27	28.54	9.5	31.46	41.3
G	9.08	13.99	7.1	14.98	65.0
T	RT	0		0	

Tab. 7 Computationally derived elastic constants of $MgSO_4 \cdot 7H_2O$ compared to the experimental data by Alexandrov et al. (1963). Temperatures are in K, all other values in GPa. Diff % gives the deviation of the preceding value from the corresponding experimental value in %.

The computationally derived elastic constants are systematically overestimated by both the PBEsol and PBE + TS approach. The PBE + TS approach performed better with a MUD on the elastic constants of 40.2% compared to 43.0 % for the PBEsol functional (Tab. 7). Regarding the effect of temperature, Stojanoff & Missell (1982) have reported the elastic constants for topologically related α-$NiSO_4 \cdot 6H_2O$ to increase on average by 10.2 % of upon cooling from 300 K to 4.2 K. Assuming a similar increase for $MgSO_4 \cdot 7H_2O$ combined with the systematic overestimation by both PBEsol and PBE + TS, would naturally improve the performance.

Comparing the performance to other studies on hydrated sulfate minerals we note that, Arbeck et al. (2010) obtained MUDs of 11.1% and 12.6% as achieved with the PBEsol xc functional when compared to elastic reference constants experimentally determined for α-$NiSO_4 \cdot 6H_2O$ by Stojanoff and Missell (1982) at 300 K and 4.2 K, respectively. We suggest that the better performance achieved by Arbeck et al. (2010) likely originates from the higher symmetry of tetragonal α-$NiSO_4 \cdot 6H_2O$ as compared to orthorhombic $MgSO_4 \cdot 7H_2O$, inevitably resulting in a less complex anisotropy of the materials properties (Neumann, 1885).

The compressional anisotropy was further assessed in terms of seismic wave velocities. The relative acoustic velocities as computed from the DFT derived elastic constants appear to be in good agreement, albeit systematically overestimated. In more detail, however, the slow secondary acoustic velocities disagree notably with the experimental data. The wave velocities in direction of the principal axis are well reproduced, in the

589 <110> direction, however, the computed shear waves are overestimated with respect to their axial values (Fig.
590 8). Lastly, the DFT calculations do not well reproduce the P wave velocity along the principal axis and
591 overestimate the velocity parallel to <100>. This failure clearly stems from the inaccurate modelling of the
592 longitudinal elastic constants as noted above. MUDs on the seismic wave speeds of 18.52 % (P, PBE + TS),
593 24.56 % (*S*, PBE + TS) 19.83 (*P*, PBEsol), and 25.80 % (*S*, PBEsol) compare very well, and in fact slightly
594 exceed the performance achieved for benzene, however, while for benzene PBEsol and PBE + TS are over-
595 and underestimating the wave velocities, respectivly, this quantity is systematically ovestimated for epsomite
596 regardless of the applied combination. Clearly, the accuracy achieved in this study is not suffiecient to be used
597 as reference in an elasticity database used for the seismic expoloration icy satellites.

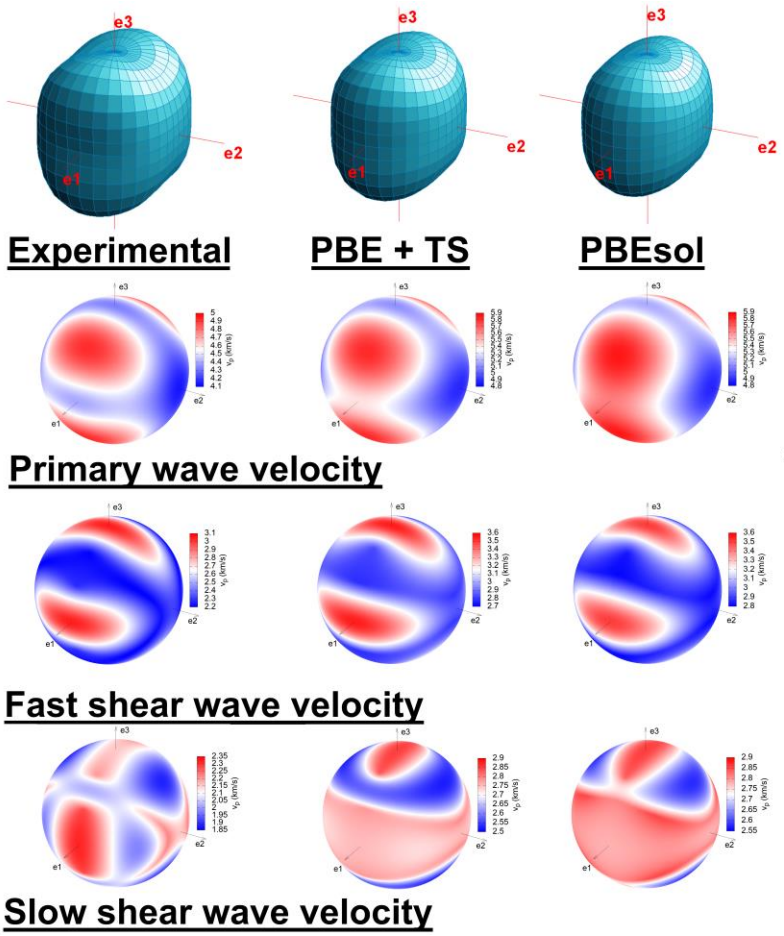

598

599 **Fig. 8** Representation surfaces of the longitudinal effect of the elastic stiffness of $MgSO_4 \cdot 7H_2O$. Clearly, the overall agreement between theory and
600 experiment is satisfactory. The seismic wave velocities however demonstrates that subtle details such as the Primary wave velocities in <100> and the
601 slow shear wave velocities in <110> are not well reproduced by the DFT calculations.

3.4. $CaSO_4 \cdot 2H_2O$

The mineral gypsum ($CaSO_4 \cdot 2H_2O$; space group: *C*2/*c*) constitutes a major of part of the sulfate fraction of carbonaceous chondrites (Kargel, 1991), which are believed to be the fundamental building blocks to have formed the icy satellites in the outer solar system (Mueller & McKinnon, 1988). Thus it would appear obvious, that $CaSO_4 \cdot 2H_2O$ is a promising candidate to constitute the non-icy materials in the salty crust and mantle of these planetary bodies, however, the mobility of $CaSO_4 \cdot 2H_2O$ is limited by its low solubility. Nevertheless, Kargel et al. (2000) suggested that $CaSO_4 \cdot 2H_2O$ might be leached from the primordial chondritic material in high-temperature environments such as in the vicinity of hydrothermal vents. Due to the high thermal gradient in these environments, $CaSO_4 \cdot 2H_2O$ would re-precipitate as the salty water cools down, potentially forming extensive deposits. If these scenario is true, $CaSO_4 \cdot 2H_2O$ could be an indicator mineral for hydrothermal vents, which support thriving ecosystems on Earth (Corliss et al., 1979) and may also be present on the Saturnian satellite Enceladus (Waite et al., 2017), under whose presumed ocean conditions life has been demonstrated to persist (Taubner et al., 2018). Moving onwards to less speculative grounds, $CaSO_4 \cdot 2H_2O$ is also an excellent choice for this high-pressure benchmarking study, due to its monoclinic symmetry requiring the determination of 13 independent elastic constants to fully account for its elastic anisotropy making it a sensitive benchmark.

The zero pressure athermal performance was evaluated against the crystal structure as determined by Schofield et al. (1996) at 4.2 K (Fig. 9). The benchmarking reveals that all but the non-dispersion corrected PBE are prone to cancellations as reflected by an excellent MSiD and much poorer MUD. PBE + TS comes out as the top performing functional having a MUD on the lattice parameters of 0.56 %, closely followed by the PBEsol, and PBE + MBD combination. The PBE + D2 is the worst performing approach, with its MUD even exceeding the non-dispersion corrected PBE functional. We further note that while PBE based approaches systematically underestimate the lattice parameters, the contrary holds for combinations involving the PBEsol xc functional.

We went on to compare our results to the DFT study of gypsum by Khalkhali et al. (2019) which have applied the PBE, PBE + D2 and PBE + TS combinations also using the Castep code and ultrasoft pseudopotentials. MUDs of 1.640, 1.168 and 0.578 % as obtained for PBE, PBE + D2, PBE + TS by Khalkhali et al., 2019 are systematically higher than the ones obtained in this study (i.e. MUD 1.014, 1.069, 0.563 %). The reason for this is likely the largely differing choice of the plane wave basis sets i.e., ~0.07 $Å^{-1}$ Brillouin zone sampling and a cut-off = 340 eV compared to ~0.03 $Å^{-1}$ and 1300 eV as used in this study. From the convergence testing (supplementary data) it is obvious, that the Brillouin zone sampling as applied by Khalkhali et al. (2019) is not sufficient to obtain well converged optimisations.

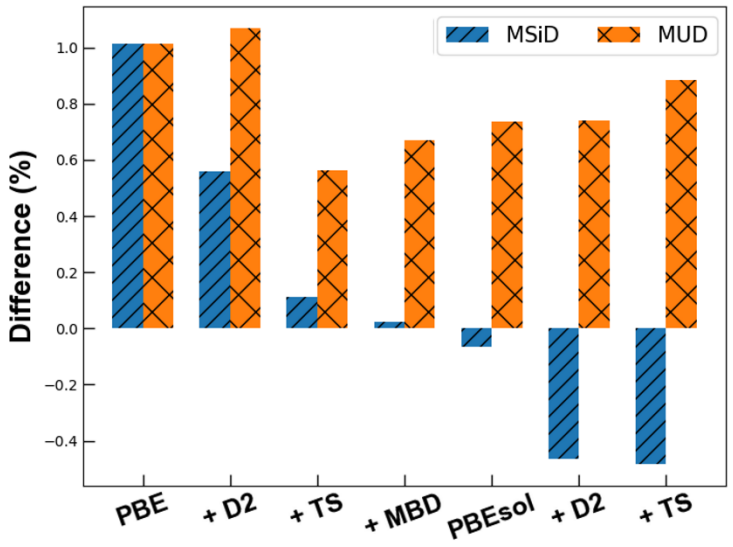

Fig. 9 MSiD (blue) and MUD (orange) of the DFT lattice vectors of $CaSO_4 \cdot 2H_2O$ benchmarked against the values determined at 4.2 K (Schofield et al., 1996) for the deuterated isotopologue..

The compressibility of $CaSO_4 \cdot 2H_2O$ has been studied in a piston cylinder experiment by Vaidya et al. (1973), in a time-of-flight neutron powder diffraction experiment involving a Paris-Edinburgh press (Stretton et al., 1997) on the deuterated isotopologue, and in diamond anvil cell experiments by Huang et al. (2000) and Comodi et al. (2008). The compressive parameters as reported by Comodi et al. (2008) and Stretton et al. (1997) are in excellent mutual agreement, but contradict those reported by Huang et al. (2000) and Vaidya et al. (1973). As pointed out by Comodi et al. (2008), the reason for the overestimation of the bulk modulus in the Huang et al. (2000) study likely originates from preferred orientation of the crystallites in the diamond

644 anvil cell powder diffraction experiment. Vaidya et al. (1973) point out that their experiments systematically
645 underestimated bulk moduli for several materials under investigation, which they attribute the closing of pores
646 of the powder sample during compression, naturally most pronounced at low pressures. We conclude that
647 Comodi et al. (2008) reported the most accurate compressive parameters for $CaSO_4 \cdot 2H_2O$ along the room
648 temperature isotherm. Noteworthy, despite this large body of experimental high-pressure studies, there is not
649 a single low-temperature compression study. For this reason, the Comodi et al. (2008) data set was used as
650 reference for the benchmarking study and the influence of thermal motion onto the compressibility will be
651 discussed accordingly.

652 The average density difference of merely 0.013 g/cm^3 the PBE + D2 approach agrees best with the
653 experimental reference profile (Fig. 10), and also demonstrates excellent performance in the relative
654 compressibility category, being almost on par with the PBE xc functional. Again, PBE performs very well
655 when benchmarked against room temperature data, albeit systematically overestimating the unit-cell volume.
656 Surprisingly, the inclusion of dispersion corrections in the PBEsol calculations results in poorer performance
657 in both of the high-pressure benchmarking categories. Based on a decrease in volume of just 1.1 % upon
658 cooling from room-temperature to 4.2 K (Schofield et al., 1996) and the higher bulk modulus, we expect the
659 temperature to have a substantially lower influence on the elasticity as compared to other title compounds.

660 Furthermore, our findings were compared to previous DFT high-pressure studies on gypsum by
661 Giacomazzi & Scandolo (2010) and Li & Lee (2018) (Tab. 8). The latter studied the compressibility of gypsum
662 by applying the revPBE xc functional in conjunction with various dispersion corrections i.e. D2, and the non-
663 local dispersion corrections DF1, DF2 and vv10. The revPBE based calculations systematically underestimate
664 the bulk modulus of gypsum, yielding values of 30.9 GPa (revPBE) and 35.5 GPa (revPBE + D2), as compared
665 to 43.80 GPa (PBE, this study), 44.18 GPa (PBE + D2, this study) and the experimental value of 44(3) GPa
666 (Comodi et al., 2008). As for the revPBE in conjunction with the non-local dispersion corrections revPBE +

DF1, revPBE + DF2 and revPBE + vv10, Li & Lee (2018) report more realistic bulk moduli of 47.7, 43.2 and 40.8 GPa, respectively.

Surprisingly, Giacomazzi & Scandolo (2010) obtained a bulk modulus of 56.7 GPa for gypsum applying the non-dispersion corrected PBE functional. Their results overestimate the bulk modulus by ~30 % when compared to both our PBE and the experimentally determined value. The plane wave basis set used in their optimisations appears to be sufficiently converged and we cannot provide any explanation for the strong disagreement between the two studies.

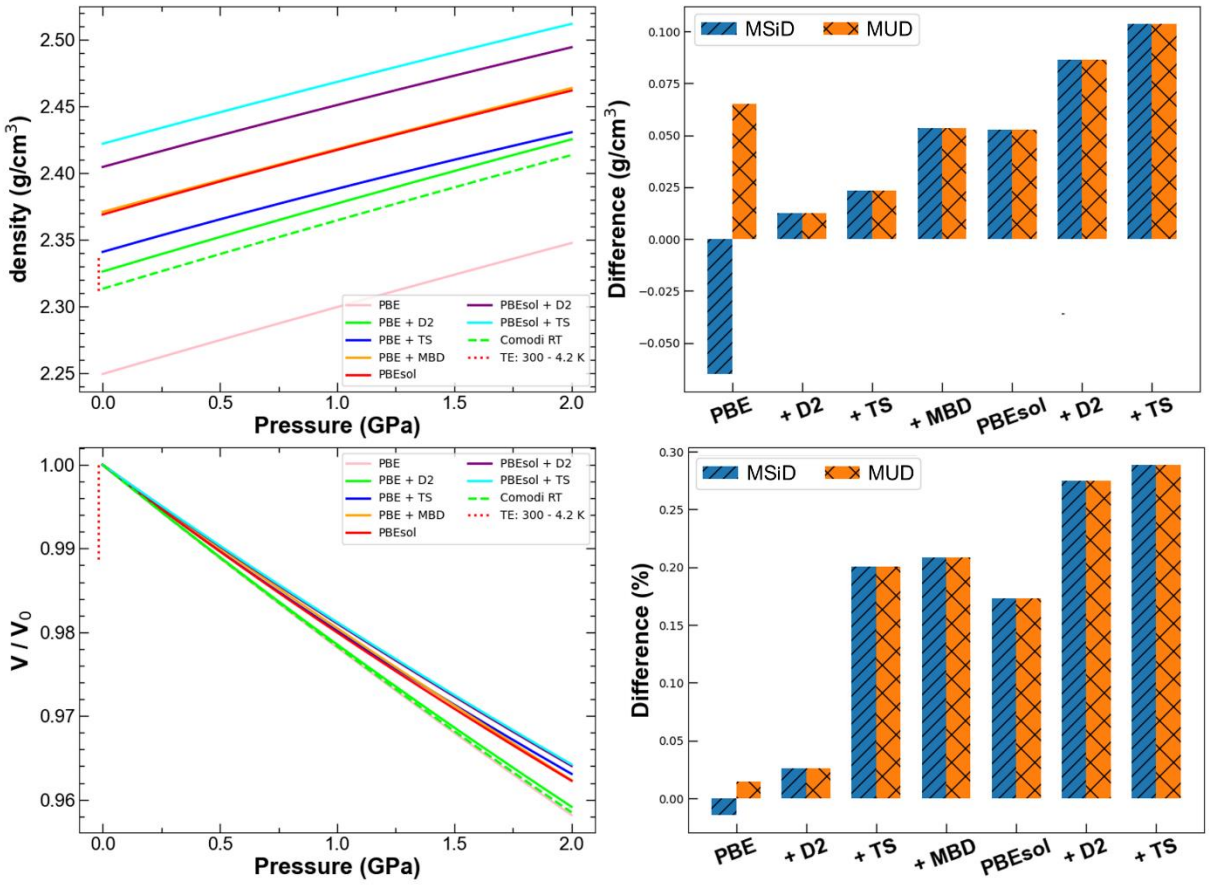

Fig. 10 Density profiles and relative compressibility of $CaSO_4 \cdot 2H_2O$ and their performance assessed in terms of MSiD and MUD. We note the excellent performance of the PBE + D2 in replicating the experimental density pressure profile as well as the relative compressibility.

V_0 (Å^3)	K (GPa)	K'	T (K)	EOS	Method	Source
508.33(15)	43.80(1.38)	3.13(1.34)	0	BM-3EOS	DFT: PBE	This study
491.55(31)	44.18(3.15)	3.94 (3.15)	0	BM-3EOS	DFT: PBE+D2	This study
488.46(2)	46.49(18)	7.19(20)	0	BM-3EOS	DFT: PBE+TS	This study
482.28(8)	49.36(1.33)	2.81(1.28)	0	BM-3EOS	DFT: PBE+MBD	This study
482.68(13)	46.77(1.51)	5.50(1.58)	0	BM-3EOS	DFT: PBEsol	This study
475.53(16)	49.89(2.12)	4.92(2.17)	0	BM-3EOS	DFT: PBEsol+D2	This study
472.11(4)	50.48(52)	4.59(52)	0	BM-3EOS	DFT: PBEsol+TS	This study
N/S	30.9	N/S	0	BM-3EOS	DFT: revPBE	Li & Lee, 2018
N/S	35.5	N/S	0	BM-3EOS	DFT: revPBE + D2	Li & Lee, 2018
N/S	47.7	N/S	0	BM-3EOS	DFT: revPBE + DF1	Li & Lee, 2018
N/S	43.2	N/S	0	BM-3EOS	DFT: revPBE + DF2	Li & Lee, 2018
N/S	40.8	N/S	0	BM-3EOS	DFT: revPBE +vv10	Li & Lee, 2018
N/S	56.7	2.2	0	Murnaghan	DFT: PBE	Giacomazzi & Scandolo, 2010
494.29(50)	44(3)	3.3(3)	RT	BM-3EOS	DAC	Comodi et al., 2008
494(3)^D	45(1)	2.0(2)	RT	BM-3EOS	NPD+PE-Press	Stretton et al., 1997
495.1(0.6)	52	N/S	RT	N/S	DAC	Huang et al., 2000
493.56	39.43	8.22	RT	Murnaghan	Piston cylinder	Vaidya et al., 1973

Tab. 8 Computationally derived athermal bulk moduli of $CaSO_4 \cdot 2H_2O$ from this study and the literature compared to the experimental values. Bulk moduli from speed of sound measurements are Voigt-Reuss-Hill averages whereas the ones derived from isothermal compression series are adiabatic. N/S denotes that this information is not stated by these authors ^{D} deuterated isotopologue.

The elasticity of gypsum has been studied by Haussühl (1965) at 273 and 293 K. It is noteworthy the choice of the crystallographic axis by Haussühl (1965) the *a* and *c* axis are inverted relative to the Comodi et al. (2008) setting, which has been used throughout this study. For this reason, we have transformed the elastic constants as reported by Haussühl (1965) accordingly (i.e., $C_{11} \Leftrightarrow C_{33}$, $C_{23} \Leftrightarrow C_{21,}$ …) for our benchmarking purposes.

Complete sets of elastic constants were computed using the PBEsol and PBE + D2 combinations (Tab. 9). The large negative values for the coupling constants C_{15} and C_{35} are well reproduced in the DFT calculations. For the small and negative C_{46} coefficient however, we obtain values of approximately the same magnitude but opposite sign. Haussühl (1965) reported a decrease of the magnitude of the C_{46} coefficient upon cooling to 273 K. Extending this trend to lower temperatures one might suggest that the opposite signs observed in theory and experiment might not be a failure of the DFT calculations, but indicate a real change of the sign of the constant C_{46} upon cooling.

The magnitude of the longitudinal elastic constants is well reproduced, but the modelling of the elastic anisotropy clearly is not satisfactory (Fig. 11). In detail, both DFT and the experimental data yield C_{33} to be the stiffest constant (Tab. 9). As for C_{22} and C_{33}, however, DFT disagrees with the experimental data yielding larger magnitudes for C_{22} than C_{11}. Due to the reference data being collected at temperatures far from 0 K,

again, we can merely speculate if this disagreement is a failure of the DFT calculations in reproducing the elasticity or if the relative magnitude of the longitudinal elastic constants indeed changes at lower temperatures. We want to note, that Haussühl (1965) report C_{22} to increase almost twice as much as C_{33} upon cooling, hence we suggest that a real change might at least be in the realm of possibilities.

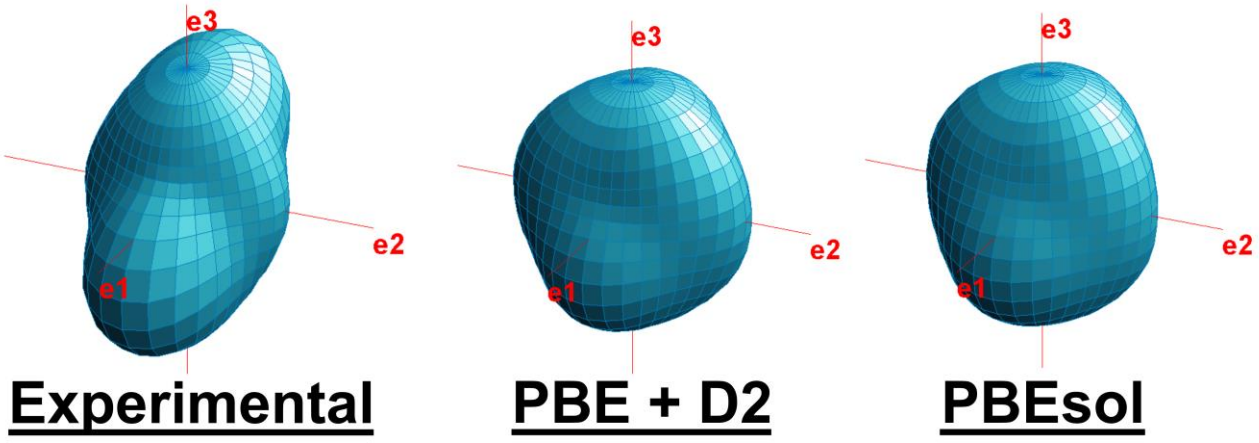

Fig. 11 Representation surfaces of the longitudinal effect of the elastic stiffness of $CaSO_4 \cdot 2H_2O$. Neither of the DFT approaches reproduces the anisotropy well.

Obviously, this disagreement in the longitudinal constants as derived by experiment and DFT is also reflected in the anisotropy of the seismic wave propagation (supplementary material: Fig. s2). However, the coupling elastic constants arising for monoclinic symmetry complicate the relationship between the elastic constants and seismic wave velocities even in the direction of the principal axes. For this reason, we constrain ourselves to assessing the magnitude of the disagreement between experiment and DFT for each of the crystal directions.

Most recently, Winkler & Milman (2019) have assessed the accuracy of PBE + D2 and PBE + TS in modelling the elastic constants of various low-symmetry dispersion dominated organic compounds. The average differences of the elastic constants (coupling coeffients omitted) relative to the experimental reference data as obtained for gypsum in this study i.e., PBEsol (33.9 %) and PBE + D2 (28.1%), compares very well

with values of 30.5 %, 37.0 % and 40.3 % as obtained by Winkler & Milman (2019) using the PBE + D2 approach for monoclinic melamine, tolane and aspirin, respectively.

PBEsol and PBE + D2 produce essentially identical seismic wave velocities overestimating the P and S wave velocities by 10.8 and 19.0 % (PBEsol), and 9.1 and 15.6 % (PBE + D2) yielding a substantial improvement in accuracy over the C_6H_6 and $MgSO_4 \cdot 7H_2O$ calculations. One reason for this might be the less pronounced temperature dependency of the stiffness, but it might also reflect a general trend of increasing accuracy as the degree of intermolecular force domination diminishes. Moreover, the relatively large error on the elastic constants of gypsum mostly stems from the inaccurate modelling of the smaller elastic constants (Tab. 9), whereas the theory and experiment agree well for the larger constants. Naturally, the larger constants will dominate the seismic wave velocities resulting in smaller overall errors on this quantity. The differences with respect to the experimental reference appear to be too large in order to be used in a reference database for elastic constants. Next to the obvious interest from a planetary science perspective, an experimental investigation of the elastic properties of gypsum at low-temperatures would be interesting in order to cast light on the origin of apparent discrepancies between theory and experiment as the observed for C_{46} constant and the relative magnitude of the longitudinal elastic constants.

C_{ij}	Exp	PBEsol	Diff %	PBE + D2	Diff %
C_{11}	72.5(3)	74.62(91)	2.9	66.79(64)	−7.9
C_{22}	62.7(3)	82.77(73)	32.0	81.89(0.52)	30.6
C_{33}	78.6(3)	90.39(1.22)	15.0	85.23(1.91)	8.4
C_{12}	24.2(2)	29.92 (32)	23.6	28.52(22)	17.9
C_{13}	26.9(3)	29.45(52)	9.5	28.80(56)	7.1
C_{23}	41.0(4)	51.34(37)	25.2	50.35(35)	22.8
C_{44}	10.4(3)	19.48(96)	87.3	16.18(1.67)	55.6
C_{55}	26.4(3)	26.56(55)	0.6	26.67(0.2)	1.0
C_{66}	9.1(3)	19.02(96)	109.0	18.33(61)	101.4
C_{15}	-17.4(5)	-10.35(27)	−40.5	-10.41(25)	−40.2
C_{25}	3.1(2)	4.19(27)	35.2	4.57(0.33)	47.4
C_{35}	-7.0(2)	-0.76(22)	−89.1	-0.43(40)	-93.9
C_{46}	-1.6(1)	0.87(36)	−154.4	1.78(30)	−211.3
K	44.22	51.07	15.5	48.49	9.7
G	17.29	21.34	23.4	19.73	14.1
T	273	0		0	

Tab. 9 Computed elastic constants of $CaSO_4 \cdot 2H_2O$ evaluated against the experimental coefficients as reported by Haussühl (1965). Temperatures are in K, all other values in GPa. Diff % gives the deviation of the preceding value from the corresponding experimental value in %

4. Summary, conclusions and outlook:

The performance of seven combinations of xc functionals and dispersion corrections (i.e. PBE, PBE + D2, PBE+TS, PBE + MBD, PBEsol, PBEsol + D2, PBEsol + TS) in replicating (i) low-temperature unit-cell shapes and (ii) bulk moduli of CO_2, C_6H_6, $MgSO_4 \cdot 7H_2O$ and $CaSO_4 \cdot 2H_2O$ was assessed. The best performing approach and the PBEsol xc functional were then used to compute the full elastic tensor, which, again, was benchmarked against experimental reference data.

The unit-cell dimensions close to the ground state were best reproduced by the dispersion corrected PBE schemes (i.e. PBE + D2, PBE + TS and PBE + MBD). PBEsol and PBE systematically overestimated the cell volumes, whereas this property was underestimated by the dispersion corrected PBEsol functional for each of the title compounds with the exception of CO_2.

The dispersion corrected PBE functionals further revealed superior performance in modelling the experimental density profiles, especially when benchmarked against experimentally determined equations of state close to the athermal limit (i.e. CO_2 and $MgSO_4 \cdot 7H_2O$). This trend is also reflected in the relative compressibility, unless benchmarked against room-temperature compression data (i.e. C_6H_6 and $CaSO_4 \cdot 2H_2O$), where the non-dispersion corrected PBEsol and PBE xc functionals exceeded, albeit systematically overestimating the density.

The best performing functional for each of the title compounds yielded MUDs of merely 0.04 g/cm^3 (CO_2), 0.02 g/cm^3 (C_6H_6), 0.003 g/cm^3 ($MgSO_4 \cdot 7H_2O$) and 0.013 g/cm^3 ($CaSO_4 \cdot 2H_2O$). We conclude that the bulk compressibility is very well reproduced by dispersion corrected DFT and may find application in exploring the compressive parameters of candidate materials which could then be used in rheological models of IOWs.

It is noteworthy, that the dispersion corrections yielded superior results for CO_2 and C_6H_6 as compared to hydrogen bonded $MgSO_4 \cdot 7H_2O$ and $CaSO_4 \cdot 2H_2O$. This is most evident when comparing $MgSO_4 \cdot 7H_2O$ and

762 C_6H_6; both exhibit orthorhombic symmetry and therefore require the same number of symmetry-independent
763 lattice parameters and elastic constants to be modelled. Next to dispersion also electrostatic, induction, and
764 exchange-repulsion components contribute to the intermolecular bonding energies (Jeziorski et al., 1994). It
765 has been demonstrated for the water dimer, which may be considered as the prototypical hydrogen bonded
766 system, that the electrostatic and exchange repulsion clearly are the dominating components of the
767 intermolecular interaction (Hoja et al., 2012). As for liquid CO_2 (Yu et al., 2011) and C_6H_6 dimers (Sherill et
768 al., 2012) dispersion is the dominating component of intermolecular interaction. Thus, it was not unexpected,
769 that we observed a better performance of dispersion corrections for the dispersion dominated as compared to
770 the hydrogen bonded solids, where other forces are likely dominating the intermolecular interaction.

771 As for the evaluation of the accuracy of DFT derived elastic tensors the scarcity of experimentally
772 elastic constants determined at low temperature is a major limitation, hindering large scale benchmarking
773 studies, which are crucial in order to detect and eventually address systematic failures of the computational
774 exploration of elastic constants using established dispersion correction schemes. Out of the four title
775 compounds, only for benzene and CO_2 could we find complete sets of elastic constants determined at low
776 temperatures, with both compounds exhibiting a dramatic increase in stiffness upon cooling, reinforcing the
777 need for accurate reference data as determined close to athermal conditions.

778 Lastly, we want to address the question raised in the introduction: Are the elastic constants computed
779 by dispersion corrected DFT accurate enough to be used in a reference data base for the seismic exploration
780 of the icy ocean worlds?

781 Despite the PBE + D2 approach having demonstrated experimental accuracy in modelling the elasticity
782 of CO_2, clearly, we have to negate this question, based on MUDs of around 10 to 25 % on the P and S wave
783 velocities as obtained for the elastically more complex title compounds. Nevertheless, DFT may play a crucial

role in determining the elastic properties of candidate materials by providing valid approximations of the elasticity, which can be used as starting values for resonant ultrasound investigations.

Regarding further potential gains in accuracy in the approximation of elastic constants from first principles we note that, Råsander & Moram (2018) observed that the GGA-type PBEsol xc functional surpasses the two hybrid functionals, PBE0 and HSE in performance, thus the use of the computationally more expensive hybrid functionals does not appear to increase the accuracy relative to the GGA-type functionals used in this study. As for the total energy method to computationally derive elastic constants, Caro et al. (2012) note that the stress-strain approach, yields identical results at lower computational cost and should therefore be chosen over the total energy method. Nevertheless, new methods for the computational approximation of elastic constants are emerging. In particular, elastic constants derived from lattice dynamic calculations from first principles as reported by Wehinger et al. (2016) yielded excellent agreement with experimentally determined elastic constants for the mineral bridgmanite, surpassing the widely used stress-strain approach following Page and Saxe (2002), which was applied in this study, in performance. We conclude that the lattice dynamics approach might open the possibility to derive more accurate elastic constants and consequently seismic wave velocities from first principles and should therefore be included in future benchmarking studies of icy satellite candidate materials.

A reference data-base of icy satellite candidate materials is still in its infancy and – due to the complex experiments involved – a rather ambitious endeavour, however, the prospect of casting light on internal structure and mantle dynamics of icy ocean worlds to eventually set constraints upon their habitability clearly makes this endeavour worthwhile.

Acknowledgement

We want to thank the editors Razvan Caracas and Alessandro Morbidelli for handling the manuscript and two anonymous reviewers for their thorough reading and constructive feedback. Computing resources

807 provided by STFC Scientific Computing Department's SCARF cluster. JMM acknowledges funding from an
808 ISIS Facility Development and Utilisation Studentship (50 %) and the University of Exeter (50 %).

809 # References:

810 Al-Saidi, W. A., Voora, V. K., Jordan, K. D., 2012. An Assessment of the vdW-TS Method for Extended Systems. J. Chem. Theory Comput. 8(4),
811 1503–1513. https://doi.org/10.1021/ct200618b

812 Alexandrov, K.S., Rhyzhova, T.V., Rostuntseva, A. I., 1963. Elastic properties of some sulfate heptahydrate crystals. Sov. Phys. Crystallogr. 7, 753-
813 755.

814 Ambrosetti, A., Reilly, A. M., DiStasio, R. A., & Tkatchenko, A., 2014. Long-range correlation energy calculated from coupled atomic response
815 functions. J. Chem. Phys. 140(18), 18A508. https://doi.org/10.1063/1.4865104

816 Arbeck, D., Haussuehl, E., Bayarjagal, L., Winkler, B., Paulsen, N., Haussuehl, S., Milman, V., 2010. Piezoelastic properties of retgersite determined
817 by ultrasonic measurements. European Phys. J. B. 73,167–175.

818 Arbeck, D., Haussuhl, E., Winkler, B., Paulsen, N., Haussuhl, S., Milman, V., & Gale, J., 2012. Elastic stiffness coefficients of thenardite and their
819 pressure and temperature dependence. Z Kristallogr. 227, 503. https://doi.org/10.1524/zkri.2012.1476

820 Birch, F., 1947. Finite Elastic Strain of Cubic Crystals. Phys. Rev. 71(11), 809–824. https://doi.org/10.1103/PhysRev.71.809

821 Bland, M. T., Singer, K. N., McKinnon, W. B., and Schenk, P. M., 2012. Enceladus' extreme heat flux as revealed by its relaxed craters, Geophys.
822 Res. Lett. 39, L17204, doi:10.1029/2012GL052736.

823 Bonev, S. A., Gygi, F., Ogitsu, T., Galli, G., 2003. High-Pressure Molecular Phases of Solid Carbon Dioxide. Phys. Rev. Lett. 91(6), 65501.
824 https://doi.org/10.1103/PhysRevLett.91.065501

825 Bridgman, P. W., 1914. Change of Phase under Pressure. I. The Phase Diagram of Eleven Substances with Especial Reference to The Melting Curve.
826 Phys. Rev. 3(3), 153–203. https://doi.org/10.1103/PhysRev.3.153

827 Bridgman, P. W., 1949. Linear Compressions to 30.000 Kg/Cm^2, including Relatively Incompressible Substances. P. Am. Acad. Arts. Sci., *77*(6),
828 189–234. https://doi.org/10.2307/20023541

829 Brown, M. E., Hand, K. P., 2013. Salts and Radiation Products on the Surface of Europa. Astron. J. 145(4), 110. https://doi.org/10.1088/0004-
830 6256/145/4/110

831 Burke, K., 2012., Perspective on Density Functional Theory. J. Chem. Phys. 136, 150901. https://doi.org/10.1063/1.4704546

832 Byrne, S., Ingersoll, A. P., 2003. A Sublimation Model for Martian South Polar Ice Features. Science. 299(5609), 1051 LP – 1053.
833 https://doi.org/10.1126/science.1080148

834 Caldeweyher, E., Bannwarth, C., Grimme, S., 2017. Extension of the D3 dispersion coefficient model. J. Chem. Phys. 147(3), 34112.
835 https://doi.org/10.1063/1.4993215

836 Calzetti, D., 2011. Polycyclic Aromatic Hydrocarbons as Star Formation Rate Indicators. EAS Publications Series. 46, 133–141.
837 https://doi.org/10.1051/eas/1146014

838 Caro, M., Schulz, S., O'Reilly, E., 2012. Comparison of stress and total energy methods for calculation of elastic properties of semiconductors. J.
839 Phys.-Condens. Mat. 25. 025803. 10.1088/0953-8984/25/2/025803.

840 Cernicharo, J., Heras, A. M., Tielens, A. G. G. M., Pardo, J. R., Herpin, F., Guélin, M., Waters, L. B. F. M., 2001. Infrared Space
841 Observatory'sDiscovery of C_4H_2, C_6H_2, and Benzene in CRL 618. Astrophys. J. 546(2), L123–L126. https://doi.org/10.1086/318871

842 Clark, S., Segall, M., Pickard, C., Hasnip, P., Probert, M., Refson, K., Payne, M. 2005. First principles methods using CASTEP. Z. Kristallogr. 220.
843 https://doi.org/10.1524/zkri.220.5.567.65075

Comodi, P., Nazzareni, S., Francesco, P., & Speziale, S. (2008). High-pressure behavior of gypsum: A single-crystal X-ray study. Am. Mineral. 93, 1530–1537. https://doi.org/10.2138/am.2008.2917

Comodi, P., Stagno, V., Zucchini, A., Fei, Y., Prakapenka, V., 2017. The compression behavior of blödite at low and high temperature up to ~10GPa: Implications for the stability of hydrous sulfates on icy planetary bodies. Icarus, 285, 137–144. https://doi.org/https://doi.org/10.1016/j.icarus.2016.11.032

Corliss, J. B., Dymond, J., Gordon, L. I., Edmond, J. M., von Herzen, R. P., Ballard, R. D., Green, K., Williams, D., Bainbridge, A., Crane, K., van Andel, T. H., 1979. Submarine Thermal Springs on the Galápagos Rift. Science. 203(4385), 1073-1083. https://doi.org/10.1126/science.203.4385.1073

Cornelius, S., Castagna, J., 2017. Variation in salt-body interval velocities in the deep-water Gulf of Mexico: Keathley Canyon and Walker Ridge areas. Interpretation. 6, 1–40. https://doi.org/10.1190/int-2017-0069.1

Cruikshank, D. P., et al., 2010. Carbon dioxide on the satellites of Saturn: Results from the Cassini VIMS investigation and revisions to the VIMS wavelength scale. Icarus. 206(2), 561–572. https://doi.org/https://doi.org/10.1016/j.icarus.2009.07.012

Csonka, G. I., Ruzsinszky, A., Perdew, J. P., Grimme, S., 2008. Improved Description of Stereoelectronic Effects in Hydrocarbons Using Semilocal Density Functional Theory. J. Chem. Theory Comput. 4(6), 888–891. https://doi.org/10.1021/ct800003n

Cybulski, S. M., Lytle, M. L., 2007. The origin of deficiency of the supermolecule second-order Møller-Plesset approach for evaluating interaction energies. J. Chem. Phys. 127(14), 141102. https://doi.org/10.1063/1.2795693

D'Hendecourt, L. B., Jourdain de Muizon, M., 1989. The discovery of interstellar carbon dioxide. Astron. Astrophys. 223, L5–L8.

Drilleau, M., Samuel,H., Rivoldini,A., Panning,M., Lognonné, P., 2021. Bayesian inversion of the Martian structure using geodynamic constraints, Geophys. J. Int. ggab105, https://doi.org/10.1093/gji/ggab105

Dubrovinsky, L., Dubrovinskaia, N., 2007. Melting of ice VII and new high-pressure, high-temperature amorphous ice. Special Paper of the Geological Society of America. 421, 105-113. 10.1130/2007.2421(07).

Earle, A., Binzel, R., Young, L., Stern, S.A., Ennico, K., Grundy, W., Olkin, C., Weaver, H.A., 2016. Long-term surface temperature modeling of Pluto. Icarus. 287. 10.1016/j.icarus.2016.09.036.

Eisenschitz, R., London, F., 1930. Über das Verhältnis der van der Waalsschen Kräfte zu den homöopolaren Bindungskräften. Z. Phys. 60(7), 491–527. https://doi.org/10.1007/BF01341258

Ende, M., Kirkkala, T., Loitzenbauer, M., Talla, D., Wildner, M., Miletich, R., 2020. High-Pressure Behavior of Nickel Sulfate Monohydrate: Isothermal Compressibility, Structural Polymorphism, and Transition Pathway. Inorg. Chem. 59(9), 6255–6266. https://doi.org/10.1021/acs.inorgchem.0c00370

Ferche, J., 1891., Ueber einige physikalische Eigenschaften des Benzols. Ann. Phys. 280, 265–287.

Figuière, P., Fuchs, A. H., Ghelfenstein, M., Szwarc, H., 1978. Pressure-volume-temperature relations for crystalline benzene. J. Phys. Chem. Solids. 39(1), 19–24. https://doi.org/https://doi.org/10.1016/0022-3697(78)90193-2

Fischer, M., Angel, R. J., 2017. Accurate structures and energetics of neutral-framework zeotypes from dispersion-corrected DFT calculations. J Chem. Phys. 146(17), 174111. https://doi.org/10.1063/1.4981528

Formalik, F., Fischer, M., Rogacka, J., Firlej, L., & Kuchta, B., 2018. Benchmarking of GGA density functionals for modeling structures of nanoporous, rigid and flexible MOFs. J. Chem. Phys, 149(6), 64110. https://doi.org/10.1063/1.5030493

Fortes, A D, Capelli, S. C., 2018. H/D isotope effect on the molar volume and thermal expansion of benzene. Phys. Chem. Chem. Phys. 20(24), 16736–16742. https://doi.org/10.1039/C8CP02500B

Fortes, A. D., Choukroun, M., 2010. Phase Behaviour of Ices and Hydrates. Space Sci. Rev. 153(1), 185–218. https://doi.org/10.1007/s11214-010-9633-3

Fortes, A. D., Knight, K. S.,Wood, I. G., (2017). Structure, thermal expansion and incompressibility of $MgSO_4 \cdot 9H_2O$, its relationship to meridianiite ($MgSO_4 \cdot 11H_2O$) and possible natural occurrences. Acta Crystallogr. B.*73*(1), 47–64. https://doi.org/10.1107/S2052520616018266

Fortes, A. D, Wood, I. G., Alfredsson, M., Vocadlo, L., Knight, K. S., 2006. The thermoelastic properties of $MgSO_4{\cdot}9D_2O$ (epsomite) from powder neutron diffraction and ab initio calculation. Eur. J. Mineral. 18(4), 449–462. https://doi.org/10.1127/0935-1221/2006/0018-0449

Giacomazzi, L., Scandolo, S., (2010). Gypsum under pressure: A first-principles study. Phys. Rev. B, 81(6), 64103. https://doi.org/10.1103/PhysRevB.81.064103

Giordano, V. M., Datchi, F., Gorelli, F. A., Bini, R., 2010. Equation of state and anharmonicity of carbon dioxide phase I up to 12 GPa and 800 K. J. Chem. Phys. 133(14), 144501. https://doi.org/10.1063/1.3495951

Gonzalez-Platas, J., Alvaro, M., Nestola, F., Angel, R., 2016. EosFit7-GUI: a new graphical user interface for equation of state calculations, analyses and teaching. J. Appl. Crystallogr. 49(4), 1377–1382. https://doi.org/10.1107/S1600576716008050

Gracia, L., Marqués, M., Beltrán, A., Pendás, A. M., Recio, J. M., 2004. Bonding and compressibility in molecular and polymeric phases of solid CO*2*. J. Phys. - Condens. Mat. 16(14), S1263–S1270. https://doi.org/10.1088/0953-8984/16/14/038

Grimme, S., 2006. Semiempirical GGA-type density functional constructed with a long-range dispersion correction. J. Comput. Chem. 27(15), 1787–1799. https://doi.org/10.1002/jcc.20495

Grimme, S., Antony, J., Ehrlich, S., Krieg, H., 2010. A consistent and accurate ab initio parametrization of density functional dispersion correction (DFT-D) for the 94 elements H-Pu. J. Chem. Phys. 132(15), 154104. https://doi.org/10.1063/1.3382344

Grimme, S., Hansen, A., Brandenburg, J. G., Bannwarth, C., 2016. Dispersion-Corrected Mean-Field Electronic Structure Methods. Chem. Rev. 116(9), 5105–5154. https://doi.org/10.1021/acs.chemrev.5b00533

Gromnitskaya, E., Yagafarov, O., Lyapin, A., Brazhkin, V., Wood, I., Tucker, M., Fortes, A., 2013. The high-pressure phase diagram of synthetic epsomite ($MgSO_4{\cdot}7H_2O$ and $MgSO_4{\cdot}7D_2O$) from ultrasonic and neutron powder diffraction measurements. Phys. Chem. Min. 40. https://doi.org/10.1007/s00269-013-0567-7

Grundy, W. M., Young, L. A., Spencer, J. R., Johnson, R. E., Young, E. F., Buie, M. W., 2006. Distributions of H_2O and CO_2 ices on Ariel, Umbriel, Titania, and Oberon from IRTF/SpeX observations. Icarus, 184(2), 543–555. https://doi.org/https://doi.org/10.1016/j.icarus.2006.04.016

Haussühl, S., 1965. Elastische und thermoelastische Eigenschaften von $CaSO_4$ $2H_2O$ (Gips). Z Kristallogr. 122(3–4), 311–314. https://doi.org/https://doi.org/10.1524/zkri.1965.122.3-4.311

Heseltine, J. C. W., Elliott, D. W., Wilson, O. B., 1964. Elastic Constants of Single Crystal Benzene. J. Chem. Phys. 40 , 2584-2587 (1964) https://doi.org/10.1063/1.1725566

Heydweiller, A., 1897. Die Erstarrungscontraction für einige organische Verbindungen. Ann. Phys. 297(7), 527–540. https://doi.org/doi:10.1002/andp.18972970707

Hohenberg, P., Kohn, W., 1964. Inhomogeneous Electron Gas. Phys. Rev. 136(3B), B864–B871. https://doi.org/10.1103/PhysRev.136.B864

Hoja, J., Sax, A.F., Szalewicz, K., 2014. Is Electrostatics Sufficient to Describe Hydrogen-Bonding Interactions?. Chem. Eur. J., 20: 2292-2300. https://doi.org/10.1002/chem.201303528

Huang, E., Xu, J.-A., Lin, J.-F., Hu, J.-Z., 2000. Pressure-induced phase transitions in gypsum. High Pressure Res. 17(1), 57–75. https://doi.org/10.1080/08957950008200306

Jaeken, J., Cottenier, S., 2016. Solving the Christoffel equation: Phase and group velocities. Computer Physics Communications, 207. https://doi.org/10.1016/j.cpc.2016.06.014

Jeziorski, B.,Moszynski, R., Szalewicz, K., 1994. Perturbation Theory Approach to Intermolecular Potential Energy Surfaces of van der Waals Complexes. Chem. Rev. 94(7), 1887-1930, doi: 10.1021/cr00031a008

Johnson, R. E., 1996. Sputtering of ices in the outer solar system. Rev. Mod. Phys., 68(1), 305–312. https://doi.org/10.1103/RevModPhys.68.305

Jones, I., Davison, I., 2014. Seismic imaging in and around salt bodies. Interpretation, *2*, SL1–SL20. https://doi.org/10.1190/INT-2014-0033.1

Kaminski, W., 2014. WinTensor (1.5). http://cad4.cpac.washington.edu/ WinTensorhome/WinTensor.htm

Knapmeyer, M., Fischer, H-H., Knollenberg, J., Seidensticker, K., Thiel, K., Arnold, W., Faber, C., Möhlmann, D., 2017. Structure and elastic parameters of the near surface of Abydos site on Comet 67P/Churyumov-Gerasimenko, as obtained by SESAME/CASSE listening to the MUPUS insertion phase. Icarus. 310. 10.1016/j.icarus.2017.12.002.

Kargel, J., Kaye, J., Head, J., Marion, G., Sassen, R., Crowley, J., Prieto-Ballesteros, O., Grant, S., Hogenboom, D., 2000. Europa's Crust and Ocean: Origin, Composition, and the Prospects for Life. Icarus, *148*, 226–265. https://doi.org/10.1006/icar.2000.6471

Kargel, J. S., 1991. Brine volcanism and the interior structures of asteroids and icy satellites. Icarus, 94(2), 368–390. https://doi.org/https://doi.org/10.1016/0019-1035(91)90235-L

Katrusiak, A., Podsiadło, M., Budzianowski, A., 2010. Association CH···π and No van der Waals Contacts at the Lowest Limits of Crystalline Benzene I and II Stability Regions. Crys. Growth Des., 10(8), 3461–3465. https://doi.org/10.1021/cg1002594

Khalkhali, M., Ma, X., Zhang, H., Liu, Q., 2019. Bulk and surface properties of gypsum: A comparison between classical force fields and dispersion-corrected DFT calculations. Comp. Mater. Sci., 164, 8–16. https://doi.org/https://doi.org/10.1016/j.commatsci.2019.03.045

Kohn, W., Sham, L. J., 1965. Self-Consistent Equations Including Exchange and Correlation Effects. Phys. Re. 140(4A), A1133–A1138. https://doi.org/10.1103/PhysRev.140.A1133

Lehmann, I., 1936. P'. Publications Du Bureau Central Seismologique International, Série A, Travaux Scientifique, *14*, 87-115.

Li, J., Sode, O., Voth, G. A., Hirata, S., 2013. A solid–solid phase transition in carbon dioxide at high pressures and intermediate temperatures. Nat. Com., 4(1), 2647. https://doi.org/10.1038/ncomms3647

Li, T.-L., Lee, P.-L., 2018. Structural evolution of gypsum under high pressure: single-crystal X-ray experiments revisited. Phys. Chem. Min. 45(9), 895–906. https://doi.org/10.1007/s00269-018-0971-0

Litasov, K. D., Inerbaev, T. M., Abuova, F. U., Chanyshev, A. D., Dauletbekova, A. K., Akilbekov, A. T., 2019. High-Pressure Elastic Properties of Polycyclic Aromatic Hydrocarbons Obtained by First-Principles Calculations. Geochem. Int. 57(5), 499–508. https://doi.org/10.1134/S0016702919050069

Liu, L., 1984. Compression and phase behavior of solid CO_2 to half a megabar. Earth Planet. Sci. Lett. 71(1), 104–110. https://doi.org/10.1016/0012-821X(84)90056-6

Lorenz, R.D., Turtle, E.P., Barnes, J.W., Trainer, M.G., Adams, D.S., Hibbard, K., Sheldon, C.Z., Zacny, K., Peplowski, P.N., Lawrence, D.J., Ravine, M.A., McGee, T.G., Sotzen, K., MacKenzie, S.M., Langelaan, J., Schmitz, S., Wolfarth, L.S., Bedini, P.D., 2018. Dragonfly: A rotorcraft lander concept for scientific exploration at titan. Johns Hopkins APL Technical Digest (Applied Physics Laboratory). 34. 374 - 387.

Malaska, M. J., Hodyss, R., 2014. Dissolution of benzene, naphthalene, and biphenyl in a simulated Titan lake. Icarus, 242, 74–81. https://doi.org/https://doi.org/10.1016/j.icarus.2014.07.022

Manzhelii, V. G., Tolkachev, A. M., Bagatskii, M. I., Voitovich, E. I., 1971. Thermal expansion, heat capacity, and compressibility of solid CO_2. Phys. Status. Solidi. B. 44(1), 39–49. https://doi.org/10.1002/pssb.2220440104

Mattsson, A., Armiento, R., Schultz, P., Mattsson, T., 2006., Nonequivalence of the generalized gradient approximations PBE and PW91. Phys. Rev. B. 73, 195123. https://doi.org/10.1103/PhysRevB.73.195123

Maynard-Casely, H. E., Hodyss, R., Cable, M. L., Vu, T. H.,Rahm, M., 2016. A co-crystal between benzene and ethane: a potential evaporite material for Saturn's moon Titan. IUCrJ, 3(3), 192–199. https://doi.org/10.1107/S2052252516002815

McCord, T B, Hansen, G. B., Clark, R. N., Martin, P. D., Hibbitts, C. A., Fanale, F. P., Granahan, J. C., Segura, M., Matson, D. L., Johnson, T. V, Carlson, R. W., Smythe, W. D., Danielson, G. E., 1998. Non-water-ice constituents in the surface material of the icy Galilean satellites from the Galileo near-infrared mapping spectrometer investigation. J. Geophys. Res-Planet. 103(E4), 8603–8626. https://doi.org/10.1029/98JE00788

McCord, T B, Hansen, G. B., Fanale, F. P., Carlson, R. W., Matson, D. L., Johnson, T. V, Smythe, W. D., Crowley, J. K., Martin, P. D., Ocampo, A., Hibbitts, C. A., Granahan, J. C., 1998. Salts on Europa'ss Surface Detected by Galileo's Near Infrared Mapping Spectrometer. Science, 280(5367), 1242 LP – 1245. https://doi.org/10.1126/science.280.5367.1242

McCord, Thomas B, Hansen, G. B., Hibbitts, C. A., 2001. Hydrated Salt Minerals on Ganymede's Surface: Evidence of an Ocean Below. Science, 292(5521), 1523. https://doi.org/10.1126/science.1059916

Meusburger, J.M., Ende, M., Talla, D., Wildner, M., Miletich, R., 2019. Transformation mechanism of the pressure-induced C2/c-to-$P1^{-}$ transition in ferrous sulfate monohydrate single crystals. J. Solid State Chem.277. https://doi.org/10.1016/j.jssc.2019.06.004

Meusburger, Johannes M., Ende, M., Matzinger, P., Talla, D., Miletich, R., Wildner, M., 2020. Polymorphism of Mg-sulfate monohydrate kieserite under pressure and its occurrence on giant icy jovian satellites. Icarus, 336, 113459. https://doi.org/10.1016/j.icarus.2019.113459

Meyer, J., 1910. Die Schmelzwaerme der Eissigsaeure, des Benzols und des Nitrobenzols. Z. Phys. Chem. 72, 225–254.

Minissale, M., Congiu, E., Manicò, G., Pirronello, A., Dulieu, F., 2013. CO_2 formation on interstellar dust grains: A detailed study of the barrier of the CO+O channel. Astron. Astrophys. 559. https://doi.org/10.1051/0004-6361/201321453

Mohorovičić, A.,1910. Potres od 8. X. 1909 (Earthquake of 8 October 1909). Godišnje izvješće Zagrebačkog meteorološkog opservatorija za godinu 1909. (in Croatian).

Monkhorst, H. J., Pack, J. D., 1976. Special points for Brillouin-zone integrations. Phys. Rev. B, 13(12), 5188–5192. https://doi.org/10.1103/PhysRevB.13.5188

Monteux, J., Golabek, G. J., Rubie, D. C., Tobie, G., Young, E. D., 2018. Water and the Interior Structure of Terrestrial Planets and Icy Bodies. Space Sci. Rev. 214(1), 39. https://doi.org/10.1007/s11214-018-0473-x

Mueller, S., McKinnon, W. B., 1988. Three-layered models of Ganymede and Callisto: Compositions, structures, and aspects of evolution. Icarus, 76(3), 437–464. https://doi.org/https://doi.org/10.1016/0019-1035(88)90014-0

Mullie, F., Reisse, J., 1987. Organic matter in carbonaceous chondrites.Organic Geo- and Cosmochemistry. 83–117.

Neumann, F. E., 1885. Vorlesungen über die Theorie der Elasticität der festen Körper und des Lichtäthers, gehalten an der Universität Königsberg, B. G. Teubner Leipzig, https://catalog.hathitrust.org/Record/008871677

Nimmo, F., 2018. Icy Satellites: Interior Structure, Dynamics, and Evolution. Oxford Research Encyclopedia of Planetary Science. https://doi.org/10.1093/acrefore/9780190647926.013.29

Olinger, B., 1982. The compression of solid CO_2 at 296 K to 10 GPa. J. Chem. Phys. 77(12), 6255–6258. https://doi.org/10.1063/1.443828

Page, Y., Saxe, P., 2002. Symmetry-General Least-Squares Extraction of Elastic Data for Strained Materials From ab Initio Calculations of Stress. Phys. Rev. B. 65, 104104. https://doi.org/10.1103/PhysRevB.65.104104

Pappalardo, R.T., et al., 2013. Science Potential from a Europa Lander, Astrobiology 13(8),740- 773, http://doi.org/10.1089/ast.2013.1003

Peeters, E. 2011. Astronomical observations of the PAH emission bands. EAS Publications Series, 46, 13–27. https://doi.org/10.1051/eas/1146002

Perdew, J. P., Burke, K., Ernzerhof, M., 1996. Generalized Gradient Approximation Made Simple. Phys. Rev. Lett, (77)18, 3865–3868.

Perdew, J. P., Ruzsinszky, A., Csonka, G. I., Vydrov, O. A., Scuseria, G. E., Constantin, L. A., Zhou, X., Burke, K. 2008. Restoring the Density-Gradient Expansion for Exchange in Solids and Surfaces. Phys. Rev. Lett., 100(13), 136406. https://doi.org/10.1103/PhysRevLett.100.136406

Pfrommer, B. G., Cote, M., Louie, S. G., Cohen, M. L., 1997. Relaxation of crystals with the quasi-Newton method. J. Comput. Phys. 131(1), 233–240. https://doi.org/10.1006/jcph.1996.5612

Powell, B. M., Dolling, G., Piseri, L., Martel, P., 1972. Normal Modes of Solid Carbon Dioxide. Neutron Inelastic Scattering Proceedings of a Symposium on Neutron Inelastic Scattering - Grenoble. 2, 207.

Prentice, A. J. R., 1993. The Origin and Composition of Pluto and Charon: Chemically Uniform Models. Pub. Astron. Soc. Aust. 10(3), 189–195. https://doi.org/DOI: 10.1017/S1323358000025649

Prentice, A.J.R., 1999. Origin, Bulk Chemical Composition And Physical Structure Of The Galilean Satellites Of Jupiter: A Post-Galileo Analysis. Earth, Moon, and Planets. 87**,** 11–55. https://doi.org/10.1023/A:1010692812892

Ringwood, A. E., 1969. Composition and Evolution of the Upper Mantle. The Earth's Crust and Upper Mantle., 1–17. https://doi.org/doi:10.1029/GM013p0001

Råsander, M., Moram, M., 2015. On the accuracy of commonly used density functional approximations in determining the elastic constants of insulators and semiconductors. J. Chem. Phys. 143. https://doi.org/10.1063/1.4932334

Schofield, P., Knight, K., Stretton, I., 1996. Thermal expansion of gypsum investigated by neutron powder diffraction. Am. Mineral. 81. 847-851, https://doi.org/10.2138/am-1996-7-807

Simon, A., Peters, K., 1980. Single-crystal refinement of the structure of carbon dioxide. Acta Cryst. B. 36(11), 2750–2751. https://doi.org/10.1107/S0567740880009879

Sherrill, C., 2012. Energy Component Analysis of π Interactions. Accounts Chem. Res. 46. 1020-1028, https://doi.org/10.1021/ar3001124.

Stähler, S. C., Panning, M. P., Vance, S. D., Lorenz, R. D., van Driel, M., Nissen-Meyer, T., Kedar, S., 2018. Seismic Wave Propagation in Icy Ocean Worlds. J. Geophys. Res. - Planet. 123(1), 206–232. https://doi.org/10.1002/2017JE005338

Staehler, S. C., et al., 2021. Seismic Detection of the Martian Core by InSight, 52nd Lunar and Planetary Science Conference, Abstract Nr. 1545

Stephenson, J., Tkalčić, H., Sambridge, M., 2021. Evidence for the innermost inner core: Robust parameter search for radially varying anisotropy using the neighborhood algorithm. J. Geophys. Res. - Sol. Ea. 126, e2020JB020545. https://doi.org/10.1029/2020JB020545

Stevenson, R., 1957. Compressions and Solid Phases of CO_2, CS_2, COS, O_2, and CO. J. Chem. Phys. 27(3), 673–675. https://doi.org/10.1063/1.1743812

Stojanoff, V., Missell, F. P., 1982. Temperature dependence of the elastic constants of α-$NiSO_4{\cdot}6H_2O$. J. Chem. Phys., 77(2), 939–942. https://doi.org/10.1063/1.443869

Stretton, I. C., Schofield, P. F., Hull, S., Knight, K. S., 1997. The static compressibility of gypsum. Geophys. Res. Lett. 24(10), 1267–1270. https://doi.org/doi:10.1029/97GL01066

Sundara Rao, R. V. G. 1950. Elastic constants of the heptahydrates of magnesium and zinc sulphate. Proc. Indian Acad. Sci. A. 31, 365–370.

Tammann, G., 1903. Kristallisieren und Schmelzen. J. A. Barth - Leipzig, 1903.

Taubner, R.-S., et al., 2018. Biological methane production under putative Enceladus-like conditions. Nat. Commun. 9(1), 748. https://doi.org/10.1038/s41467-018-02876-y

Tkatchenko, A., Scheffler, M., 2009. Accurate Molecular Van Der Waals Interactions from Ground-State Electron Density and Free-Atom Reference Data. Phys. Rev. Lett., 102(7), 73005. https://doi.org/10.1103/PhysRevLett.102.073005

Vaidya, S. N., Bailey, S., Pasternack, T., Kennedy, G. C., 1973. Compressibility of fifteen minerals to 45 kilobars. J. Geophys. Res. 78(29), 6893–6898. https://doi.org/10.1029/JB078i029p06893

Vanderbilt, D., 1990. Soft self-consistent pseudopotentials in a generalized eigenvalue formalism. Phys. Rev. B. 41(11), 7892–7895. https://doi.org/10.1103/PhysRevB.41.7892

Vinatier, S., Schmitt, B., Bézard, B., Rannou, P., Dauphin, C., Kok, R., Jennings, D. E., Flasar, F., 2017. Study of Titan's fall southern stratospheric polar cloud composition with Cassini/CIRS: Detection of benzene ice. Icarus. 310, 89-104, https://doi.org/10.1016/j.icarus.2017.12.040

Voronkov, A. A., 1958. The piezoelectric, elastic and dielectric properties of crystals of $MgSO_4$. $7H_2O$. Sov. Phys. –Crystallogr., 3, 722–725.

Vuitton, V., Yelle, R. V., Cui, J. 2008, Formation and distribution of benzene on Titan. J. Geophys. Res., 113, E05007, doi:10.1029/2007JE002997.

Waite, J. H., Glein, C. R., Perryman, R. S., Teolis, B. D., Magee, B. A., Miller, G., Grimes, J., Perry, M. E., Miller, K. E., Bouquet, A., Lunine, J. I., Brockwell, T., Bolton, S. J., 2017. Cassini finds molecular hydrogen in the Enceladus plume: Evidence for hydrothermal processes. Science, 356(6334), 155 - 159. https://doi.org/10.1126/science.aai8703

Walmsley, S. H., 1968. Excitons, Magnons, Phonons, Molecular Crystals: Proceedings of International Symposium, Edited by A. B. Zahlan; Cambridge University Press, 83.

Wang, A., Jolliff, B. L., Liu, Y., Connor, K., 2016. Setting constraints on the nature and origin of the two major hydrous sulfates on Mars: Monohydrated and polyhydrated sulfates. J. Geophys. Reas. Planet. 121(4), 678–694. https://doi.org/10.1002/2015JE004889

Wang, W., Fortes, A. D., Dobson, D. P., Howard, C. M., Bowles, J., Hughes, N. J., Wood, I. G., 2018. Investigation of high-pressure planetary ices by cryo-recovery. II. High-pressure apparatus, examples and a new high-pressure phase of $MgSO_4$. $5H_2O$. J. Appl. Crystallogr. 51(3), 692–705. https://doi.org/10.1107/S1600576718003977

Wehinger, B., Bosak, A., Nazzareni, S., Antonangeli, D., Mirone, A., Chaplot, S., Mittal, R., Ohtani, E., Shatskiy, A., Saxena, S., Ghose, S., Krisch, M., 2016. Dynamical and elastic properties of MgSiO3 perovskite (bridgmanite). Geophys. Res. Lett. 43, 2568– 2575. 10.1002/2016GL067970.

Winkler, B., Milman, V., 2014. Density functional theory based calculations for high pressure research. Z Kristallogr. - Cryst. Mater. 229(2), 112–122. https://doi.org/https://doi.org/10.1515/zkri-2013-1650

Winkler, B., & Milman, V., 2019. Accuracy of dispersion-corrected DFT calculations of elastic tensors of organic molecular structures. Cryst. Growth Des. *20*, 206–213. https://doi.org/10.1021/acs.cgd.9b01017

Yu, K., McDaniel, J., Schmidt, J., 2011. Physically Motivated, Robust, ab Initio Force Fields for CO_2 and N_2 J. Phys. Chem. B. 115., 10054- 10063. 10.1021/jp204563n.

Yoo, C. S., Cynn, H., Gygi, F., Galli, G., Iota, V., Nicol, M., Carlson, S., Häusermann, D., Mailhiot, C., 1999. Crystal Structure of Carbon Dioxide at High Pressure: ``Superhard'' Polymeric Carbon Dioxide. Phys. Rev. Lett. 83(26), 5527–5530. https://doi.org/10.1103/PhysRevLett.83.5527